PHYSICAL REVIEW B **85**, 165113 (2012)

Multiplet ligand-field theory using Wannier orbitals

M. W. Haverkort,[1] M. Zwierzycki,[2] and O. K. Andersen[1]
[1]*Max Planck Institute for Solid State Research, Heisenbergstraße 1, 70569 Stuttgart, Germany*
[2]*Institute of Molecular Physics, Polish Academy of Sciences, M. Smoluchowskiego 17, 60-179 Poznań, Poland*

(Received 21 November 2011; revised manuscript received 7 March 2012; published 9 April 2012)

We demonstrate how *ab initio* cluster calculations including the full Coulomb vertex can be done in the basis of the localized Wannier orbitals which describe the low-energy density functional (local-density approximation) band structure of an infinite crystal, e.g., the transition-metal $3d$ and oxygen $2p$ orbitals. The spatial extent of our $3d$ Wannier orbitals (orthonormalized Nth-order muffin-tin orbitals) is close to that found for atomic Hartree-Fock orbitals. We define ligand orbitals as those linear combinations of the O $2p$ Wannier orbitals which couple to the $3d$ orbitals for the chosen cluster. The use of ligand orbitals allows for a minimal Hilbert space in multiplet ligand-field theory calculations, thus reducing the computational costs substantially. The result is a fast and simple *ab initio* theory, which can provide useful information about local properties of correlated insulators. We compare results for NiO, MnO, and $SrTiO_3$ with x-ray absorption, inelastic x-ray scattering, and photoemission experiments. The multiplet ligand-field theory parameters found by our *ab initio* method agree within ∼10% with known experimental values.

DOI: 10.1103/PhysRevB.85.165113 PACS number(s): 71.70.Ch, 71.15.Qe, 71.35.−y, 78.70.Dm

I. INTRODUCTION

Many electronic properties of solids can now be described *ab initio* thanks to the advent of powerful computers and the development of ingenious methods, such as density-functional theory[1–3] (DFT) with local density[4] (LDA) or generalized gradient[5] (GGA) approximations, the LDA + Hubbard U (LDA + U),[6,7] quantum chemical methods,[8–12] dynamic mean-field theory,[13–20] quantum Monte Carlo simulations,[21,22] and exact diagonalization for finite clusters.[22,23] Nevertheless, for correlated open-shell systems with several local orbital and spin degrees of freedom, electronic-structure calculations remain a challenge.

Ground-state properties and spectral functions may be calculated by exact diagonalization of the many-electron Hamiltonian, but this is hindered by the exponential growth of the Hilbert space with the number of correlated electrons in the system. Exploiting symmetry and limiting the number of correlated electronic degrees of freedom may enable the treatment of relatively large clusters, as was done in the important case of doped high-T_c cuprates, where symmetry in the spin sector allowed Lau and co-workers to use clusters with up to 32 CuO_2 plaquettes, each with a single Cu $d_{x^2-y^2}$, and two O p orbitals.[24] For *local* properties, such as excitonic spectra, exact diagonalization for finite clusters becomes much more appealing, as relatively small clusters often suffice. Magnetic anisotropies, g tensors, magnetization-dependent electron-spin resonance spectra, crystal-field excitations, and a manifold of excitonic core-level spectra are usually well described using very small clusters. For transition-metal and rare-earth compounds, the cluster may often be limited to merely a single d- or f-electron cation surrounded by its nearest-neighbor ligands as illustrated in Fig. 1. For clusters that small, exact diagonalization is equivalent to multiplet ligand-field theory (MLFT), one of the earliest quantum-chemistry methods developed to describe the electronic structure of transition-metal and rare-earth compounds.[25] MLFT is a highly cost-efficient method, able to account for many of the local properties and excitonic spectra of correlated materials.

MLFT calculations traditionally use parameters fitted to experiments. Despite being a great help for understanding and interpreting experimental results, this approach is, however, not completely satisfactory and, over the years, numerous theoretical studies have therefore been devoted to obtaining MLFT parameters *ab initio*.[26–41] Sugano and Shulman[26] calculated the ligand-field parameters by constructing single-particle molecular orbitals (MOs) as linear combinations of atomic Hartree-Fock orbitals and thereby in several cases obtained qualitative agreement with experiments. More often, MO theory with a more complete basis is used.[29,30] After the LDA had proven useful not only for s and p, but also for d and f electrons in solids,[42] several authors obtained MLFT parameters by performing an LDA calculation for the cluster and using its Kohn-Sham MOs.[31–37] Such a calculation breaks the translation invariance of the crystal already at the single-particle LDA level, and it is necessary to remedy finite-size and surface effects, e.g., by embedding the cluster in a set of point charges mimicking the rest of the solid. Such procedures are not well controlled, e.g., depending on the details, the sign of the crystal field may change.[26–28]

Here we use a different route to performing *ab initio* MLFT calculations. Our procedure is similar to the method originally devised by Gunnarsson *et al.*[43,44] for obtaining the parameters in the Anderson impurity model and, in the last 15 years, used extensively for dynamical-mean-field-theory (DMFT) calculations for realistic solids (LDA + DMFT).[16–20] We start our *ab initio* MLFT calculation by performing a DFT calculation for the proper, infinite crystal using a modern DFT code which employs an accurate density functional and basis set [e.g., linear augmented plane waves (LAPWs)].[45,46] From the (self-consistent) DFT crystal potential we then calculate *a set of Wannier functions* suitable as the single-particle basis for the MLFT calculation.[47–52] Since the members of such a set are centered on either the transition-metal (TM) or ligand atoms,

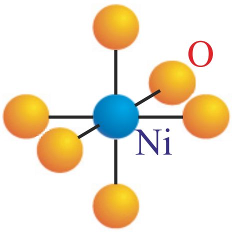

FIG. 1. (Color online) A NiO_6 cluster used in multiplet ligand-field theory (MLFT) as a local representation of the rocksalt face-centered-cubic NiO solid. The Ni cation is surrounded by its six nearest-neighbor O ligands.

we shall call them Wannier *orbitals*. Typically, they are the TM 3*d* and oxygen 2*p* orbitals which, taken together, exactly describe the DFT 3d and 2p bands. For the distinction between italic and roman fonts for p and d orbitals, see Appendix A. In general, the set should be minimal and span exactly all DFT solutions in the energy range relevant for the property to be calculated. It is important that this set contains sufficiently many ligand orbitals to make the correlated TM orbitals well localized, i.e., the TM *d* orbitals should not have tails on any other atom. This localization allows one to restrict the many-electron calculations of local properties to a single TM site plus its ligand neighbors. Hence, in the current method, there are no embedding errors, except those arising from truncating the single-particle basis to include only the Wannier orbitals on the cluster.

In the following we introduce the method by the example of the late transition-metal oxide NiO with configuration $3d^8$. In Sec. II, we show that similar results can be obtained for middle and early transition-metal oxides, specifically $3d^5$ MnO and $3d^0$ $SrTiO_3$.

In Sec. III, we compare with results obtained by several different experimental techniques: (Sec. III A) 2*p* x-ray absorption (XAS), a charge-neutral excitation of a transition-metal 2*p* core electron into the 3*d* shell; (Sec. III B) 2*p* core-level x-ray photoemission (XPS) from Ni impurities in MgO; (Sec. III C) inelastic x-ray scattering (IXS) of core to valence excitations, a technique similar to XAS; we specifically show 3*p* core-electron excitations into the 3*d* shell; (Sec. III D) inelastic x-ray scattering of *d*-*d* excitations. The experiments presented for these materials are relatively well understood, so that the comparison with our *ab initio* results constitute a critical test of the theoretical method. At the end of the paper, we give our conclusions. In Appendix A we provide information on the different basis sets or Wannier orbitals used, as well as the meaning of the different occupation numbers and the concept of formal valence. Details of the calculations, including numerical values of several MLFT parameters obtained *ab initio,* may be found in Appendix B. A discussion of the double counting of interactions in the LDA and MLFT calculations may be found in Appendix C. In Appendix D we show how ligand orbitals can be obtained in general symmetry from the O 2*p* orbitals, with the use of block tridiagonalization of the orbital basis set. This is an essential ingredient which makes these calculation numerically efficient. Appendix E contains a short note on the exact diagonalization routines.

II. OBTAINING THE MLFT PARAMETERS FROM THE LDA BY THE EXAMPLE OF NiO

In this section we introduce the *ab initio* MLFT method by the example of NiO. We will discuss the different steps taken in order to obtain the MLFT parameters. First we discuss the LDA procedure used to obtain the potential, Wannier functions and tight-binding parameters. Next we discuss the meaning of the different one-electron parameters. In the last part of this section we discuss many-body parameters, i.e., the Slater integrals.

We start our *ab initio* calculations with a conventional charge-self-consistent LDA calculation for the experimental crystal structure. NiO has the rocksalt structure in which each Ni atom is surrounded by six O atoms in cubic symmetry, and vice versa. We used the linear augmented plane wave method[45,53] as implemented in WIEN2K.[46] The resulting LDA band structure is shown along the symmetry lines of the face-centered-cubic (fcc) Brillouin zone in Fig. 2. It is not very different from the band structure obtained and discussed 40 years ago by Mattheiss[54] who used Slater exchange and a non-self-consistent potential construction. The three O 2p bands extend over 5 eV, from −8.2 to −3.2 eV below the Fermi level. The five Ni 3d bands consist of three t_{2g} bands extending from −3.0 to −0.9 eV and two e_g bands extending from −1.4 to + 1.3 eV. The bottom of the Ni 4s band is 1.5 eV above the Fermi level and at the Γ point. As pointed out by Mattheiss, the reason why the 4s band is above the 3d bands and thus empty, while it is half full in elemental Ni, is that strong hybridization with the O 2*p* band pushes it up (and the 2*p* band down) in the oxide.

Within the LDA, NiO is a metal, in strong contrast to experiments where NiO is found to be a good insulator with a room-temperature resistance of $\sim 10^5$ Ω cm and an optical band gap of about 3.0–3.5 eV.[55–57] This is one of the most noticeable failures of the LDA. However, for the current paper, this is not a problem. Although the LDA cannot reproduce the correct electronic structure near the nickel atom, the minimal set of localized Ni *d* and O *p* orbitals which together span the low-energy solutions of Schrödinger's equation for the LDA crystal potential exactly, i.e., the $5 + 3 = 8$ bands in Fig. 2, is expected to constitute a good single-particle basis set for many-body calculations.

In order to prevent double counting of the multipole part of the Coulomb interaction, we constrain the self-consistent LDA potential to be spherically symmetric inside nonoverlapping muffin-tin (MT) spheres (see Appendixes B and C), but allow it to be general in the MT interstitial; it is a so-called *warped* MT potential. For this potential we generate a basis set of eight localized TM *d* and O *p* orbitals per cell which span the eight bands exactly. Since these bands do not cross any other bands in NiO, this can be done by projection of the LDA LAPW Bloch states onto Wannier functions choosing band- and **k**-dependent phases which make the Wannier functions atom centered and localized. For an oxide like $SrTiO_3$, the TM *d* and O *p* bands *do* cross and hybridize with other bands far away from the Fermi level; near avoided crossings it is therefore not clear onto which of the bands to project. Moreover, one might want to go beyond perfect crystals. Rather then using projection, we generate the minimal basis set of localized orbitals

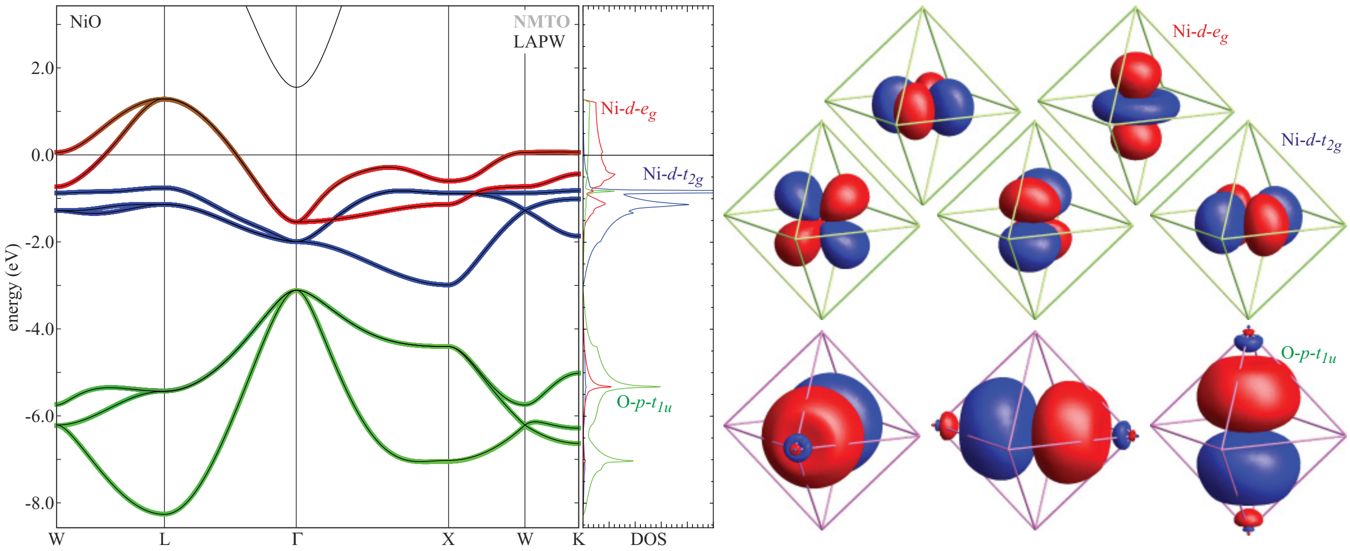

FIG. 2. (Color online) Left panel: NiO LDA band structure calculated with the large LAPW basis set (thin, black lines) and with the small Wannier-orbital basis set consisting of three O p (green), three Ni $d(t_{2g})$ (blue), and two Ni $d(e_g)$ (red) orthonormalized NMTOs per NiO (thick colored lines). Colors are mixed according to the hybridization between the Bloch sums of the three kinds of orbital. The Fermi level is taken as the zero of energy. Middle panel: Wannier-orbital projected densities of states. Right panel: The eight Wannier orbitals. Shown are constant-amplitude contours containing 90% of the orbital charge with the color (red or blue) giving the sign. The Ni(O)-centered octahedra have O(Ni) at their corners.

directly by using the Nth-order muffin-tin orbital (NMTO) method.[47–49] This method solves the problem exactly by multiple-scattering theory at $N+1$ chosen energies, followed by Nth-order polynomial interpolation in the Hilbert space, but only for a superposition of spherically symmetric short-ranged potentials (to leading order in the potential overlap). We must therefore first perform the overlapping muffin-tin approximation[58] (OMTA) to the warped MT potential, i.e., by least-squares minimization determine the radial shapes of the overlapping potential wells and the common potential zero.

The resulting basis set of five Ni d plus three O p NMTOs per cell[59,60] with the $N+1=2$ energies $\epsilon_0=-5.2$ and $\epsilon_1=-1.2$ eV produces the eight colored, thick bands in Fig. 2. Within the width of the line they are indistinguishable from the LAPW bands. Hence, the NMTO minimal basis set for the OMTA to the warped potential is a highly accurate representation of the large LAPW basis set for the low-energy states, but many times more efficient. Our Wannier orbitals are symmetrically orthonormalized NMTOs,[47–49] and the colors indicate the relative O p, Ni $d\left(t_{2g}\right)$, and Ni $d\left(e_g\right)$ Wannier-orbital characters. The middle panel of Fig. 2 shows the partial density of states projected onto these Wannier orbitals. Compared with the commonly used projection onto truncated partial waves inside a MT sphere, our projection has the advantage of leading to well-defined occupation numbers because it is onto a complete, orthonormal basis set of localized, smooth orbitals. Our projection also takes care of the O $p\,(t_{1u})$ character which flows into the neighboring Ni MT sphere due to the large size of the Wannier O p orbital. In this regard, it should be remembered that a MT sphere is not chosen to give a good representation of the charge density, and hence of the occupied Wannier orbitals, but of the *potential*. Since the latter has an envelope function which for rocksalt-structured NiO is essentially the Coulomb potential from equal but opposite point charges on identical cubic sublattices, Ni and O have *similar-sized* MT spheres. This makes it necessary for the wave functions resulting from a MT-based method for solving Schrödinger's equation, such as the LAPW method, to carry the partial-wave expansions much further than to p or d, typically to $l\sim 8$, because the outer parts of the O p orbitals, for instance, are being expanded around the Ni sites. Nevertheless, with appropriately normalized partial waves, projection of the density of states does give similar results as with Wannier pd orbitals.

The eight Wannier orbitals $w_i\,(\mathbf{r})$ are shown on the right-hand side of Fig. 2 as those surfaces where $|w_i\,(\mathbf{r})| = \mathrm{const}$ and which incorporate 90% of the charge, $\int_S |w_i\,(\mathbf{r})|^2\, d^3r \equiv 0.9$. The red or blue color of a lobe gives its sign. As one can see, the Ni d orbitals are extremely well localized. This is a necessary condition for several many-body models which implicitly assume such an orbital basis set, for example, the Hubbard model which neglects all off-site Coulomb correlations. In order to visualize the localization of the Ni 3d Wannier orbitals at a more quantitative level, we computed the effective radial wave functions for the t_{2g} and e_g orbitals by multiplying with the corresponding spherical harmonics and averaging over all solid angles. These radial functions are compared in Fig. 3 with that of a Ni atom in the d^8 configuration as calculated with the Hartree-Fock method.[61] Although there are slight differences, the agreement is astonishing. The local Ni d Wannier orbitals in NiO are rather similar to atomic Ni wave functions. Note that the atomic Ni d radial function depends on the filling of the d shell, but is rather insensitive to the filling of the 4s shell. The atomic radial function shown in Fig. 3 is calculated for a $\mathrm{Ni}^{2+}(3d^84s^0)$ configuration, but would be

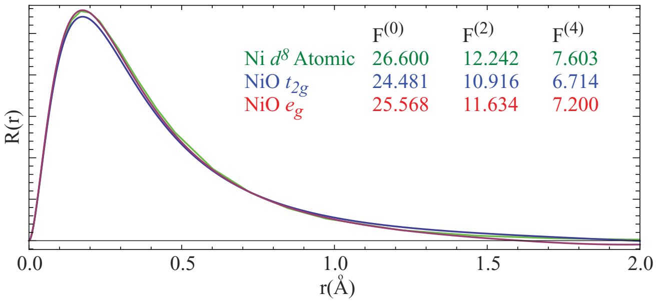

FIG. 3. (Color online) Angular-averaged radial wave functions $R(r)$ for the Ni e_g and Ni t_{2g} Wannier orbitals compared with the Hartree-Fock radial wave function for a Ni^{2+} ion in a $3d^8$ configuration. For Ni$^+$ $3d^8s^1$ and Ni $3d^8s^2$, the radial functions are similar. The distance to the nearest oxygen is 2.09 Å, which is consistent with the sum of the ionic radii of 0.72 Å for Ni^{2+} and 1.40 Å for O^{2-}. The inset shows the Slater integrals Eq. (1) for the multipole Coulomb interactions.

practically the same for a Ni$^+$ $(3d^84s^1)$ or neutral Ni $\left(3d^84s^2\right)$ configuration.

Since we have chosen not to include Ni s orbitals in the minimal basis, it does not describe the high-lying, empty Ni 4s band which has antibonding O $2p$ character. The corresponding Ni $4s$ bonding character of the O $2p$-like band is, however, completely taken care of by including (downfolding) the Ni $4s$ character into the tails of the O $2p$ Wannier orbitals, as is seen in Fig. 2. In the bottom right-hand panel one can see how Ni $4s$ character is added at the tip of each lobe of the O $2p$ orbital, such that the outermost $4s$ radial lobe expands the tip of the $2p$ lobe, while the remaining inner radial $4s$ lobes of alternating sign cause the $2p$ lobe to tail off in an oscillating manner. The shape of the O $2p$ Wannier orbital is of course also influenced by the requirement that it be orthogonal to the Ni $3d$ Wannier orbitals.

The *N*MTO method is particularly useful when a real-space tight-binding representation of the Hamiltonian is needed.[17,20,43,44,50,52] Both the orthogonal Wannier functions as well as the corresponding tight-binding representation of the Hamiltonian in this basis set are directly available in the *N*MTO formalism. Details on the *N*MTO method can be found in previous publications[47–49] and Appendix B. Here we would like to stress that the Wannier orbitals used within this paper are not constructed by maximally localizing the Wannier functions,[62] but their extent is a result of symmetry constraints. This leads to orbitals that are not always maximally localized, especially in the details of the tails of these orbitals. The Ni d Wannier orbitals obtained by *N*MTO do show a very large overlap with atomic orbitals, which might well be larger than the overlap one might find between atomic orbitals and maximally localized Wannier orbitals. It is the agreement between our Wannier orbitals and atomic orbitals which makes the method successful. An alternative method to obtain good Wannier orbitals for correlated model calculations could be to maximize the overlap of the Wannier orbital with atomic orbitals.

Although only the Ni d bands in Fig. 2 are partly occupied, inclusion of O p orbitals in the basis is important for describing spectroscopy. In photoemission, for example, the removal of a TM d electron can lead to a transfer of charge from the O to the TM atom. This dynamical screening would not be captured on a basis of only TM d orbitals. Multiplet *crystal*-field theory (MCFT), i.e., local calculations using a basis of only TM d orbitals, which have antibonding O p tails fixed to them, can be useful in many other cases, for example for calculating magnetic anisotropies. In this paper, however, we concentrate on multiplet *ligand*-field theory and explicitly include the O p orbitals in the basis set.

Until now, we have considered an infinite crystal and have calculated the one-electron potential in the local-density and warped muffin-tin approximations. For that potential we have derived a set of localized O p and Ni d Wannier orbitals which exactly describe the O p and Ni d bands, as well as the corresponding tight-binding Hamiltonian. We now use these orbitals and this Hamiltonian for the NiO$_6$ cluster (Fig. 1). The band structure thereby reduces to the O p-like π and σ levels and the Ni d-like π^* and σ^* levels shown in the central part of the left-hand panel of Fig. 4, plus some O p levels which do not couple to the Ni d levels and are therefore not shown in the figure. For comparison, we repeat from Fig. 2 the crystalline density of states projected onto the O p, Ni $d(t_{2g})$, and $d(e_g)$ orbitals. In the following we discuss the formation of these simple cluster levels before we consider calculating many-electron multiplets.

The *N*MTO Ni d Wannier orbitals have the on-site energies $\epsilon_{t_{2g}} = -1.55$ and $\epsilon_{e_g} = -1.05$ eV with respect to the Fermi level. Had the potential been spherically symmetric within the range of the Ni d orbitals, the e_g and t_{2g} radial functions in Fig. 3 would have been identical, and their levels degenerate with energy $\epsilon_d = \frac{3}{5}\epsilon_{t_{2g}} + \frac{2}{5}\epsilon_{e_g} = -1.35$ eV. The crystal-field splitting, $10Dq = \epsilon_{e_g} - \epsilon_{t_{2g}} = 0.5$ eV, is basically due to the fact that the e_g and t_{2g} orbitals point respectively toward and between the nearest oxygen neighbors, which are negatively charged. (The notation $10Dq$ for $\epsilon_{e_g} - \epsilon_{t_{2g}}$ is standard in MLFT.[63]) In the conventional ionic picture, two electrons are transferred from each neutral Ni $3d^84s^2$ atom to each O atom, where they complete the $2p$ shell. Hence, the crystal-field splitting would be the radial matrix element of the nonspherical part of the electrostatic Madelung potential proportional to $r^4\{Y_{40}(\hat{\mathbf{r}}) + \sqrt{(5/14)}[Y_{44}(\hat{\mathbf{r}}) + Y_{4-4}(\hat{\mathbf{r}})]\}$ from these ± 2 charges. However, with the atomic radial function shown in Fig. 3, which yields $\langle r^4\rangle \approx (0.71\ \text{Å})^4$, the splitting is merely $\sim$0.3 eV, i.e., $\sim$0.2 eV too small, and this is even an overestimate because the charge transfer from the 4s to the 2p band is reduced by covalency. Note in passing that, had we taken the anisotropy of the electrostatic potential to be the one caused by the LDA charge density and the protons outside the Ni MT sphere, we would have obtained merely 0.01 eV. This is so because the Ni MT radius of 1.10 Å is larger than the Ni^{2+} ionic radius of 0.72 Å and thus cuts off part of the oxygen charge density (remember that MT spheres are designed to describe the potential and not the charge density). Hence, the anisotropy experienced by the different *angular* behaviors of the e_g and t_{2g} orbitals can at most account for only half the calculated crystal-field splitting. Next, we turn to the different *radial* behaviors (Fig. 3). These are mostly due to the requirement that the Ni e_g and t_{2g} Wannier orbitals be orthogonal to the nearest O $2p$ orbitals. The e_g radial function changes sign for increasing r, while the t_{2g} radial function

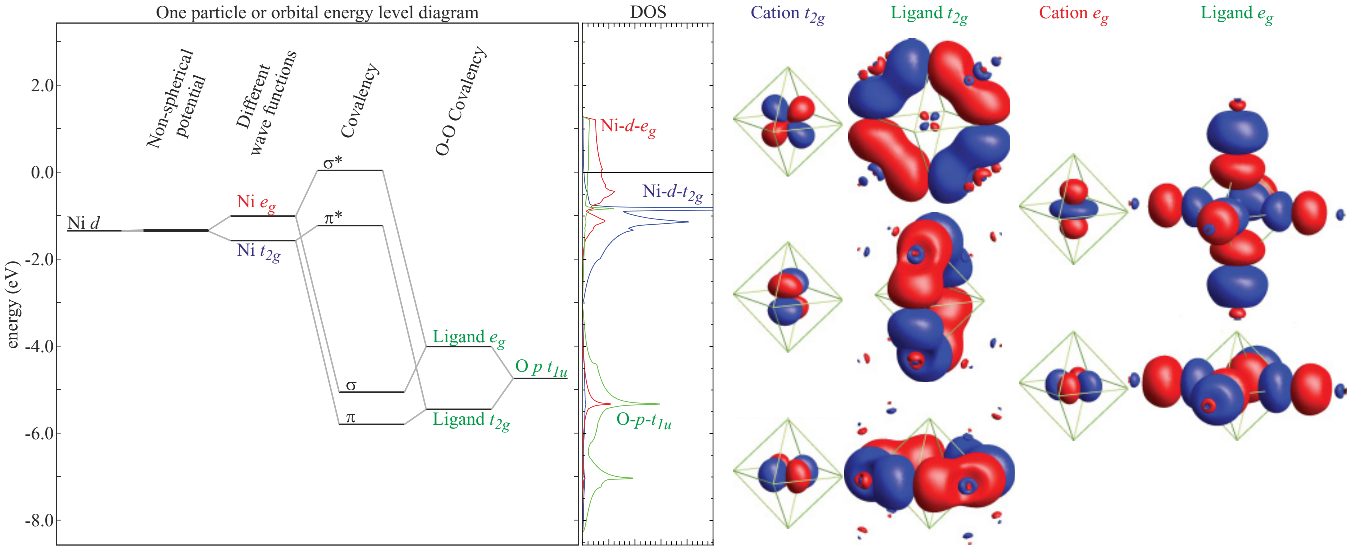

FIG. 4. (Color online) Left panel: Orbital energy-level diagram for the NiO_6 cluster on the same energy scale as the LDA band structure for the solid (Fig. 2) shown in the middle panel. The Fermi level is the zero of energy. Right panel: Constant-amplitude contours of the Ni d Wannier orbitals and of the Ni-centered ligand orbitals. The latter are symmetrized linear combinations of the O p Wannier orbitals.

merely decays. At short distances ($r \lesssim 0.7$ Å), the normalized e_g radial function is therefore larger than the normalized t_{2g} function. Since the maxima of the two radial functions occur where the radial potential $v_{\mathrm{Ni}}(r) + 6/r^2$ is huge and negative, the higher e_g maximum causes a lower potential energy, opposite to what is needed to explain the size of the crystal-field splitting. In the end, it turns out that the ~0.5 eV crystal-field splitting is not only a result of the potential acting on the different angular and radial wave functions, but also due to the *kinetic* energy. The e_g orbitals overlap more with the O p orbitals than do the t_{2g} orbitals, whereby orthogonalization increases the kinetic energy more for the former than for the latter. For the calculation of the MLFT parameters it turns out to be important to treat all these interactions on an equal footing.

We now continue our explanation of the orbital energy-level diagram in Fig. 4, this time starting from the on-site energy $\epsilon_p = -4.74$ eV of the O $2p$ Wannier orbitals marked on the right-hand side. The ionic energy is thus $\epsilon_d - \epsilon_p \approx 3.4$ eV. Since we have chosen not to include Ni $4s$ orbitals in the basis set, the bonding Ni s character has been downfolded into the O p orbitals so that the -4.75 eV includes a downward shift of about 1 eV from Ni s covalency. The NiO_6 cluster contains $6 \times 3 = 18$ O p orbitals, but not all linear combinations can interact with d orbitals on the central Ni site. Hence, the basis set for the MLFT calculations can be greatly reduced by including only those linear combinations which do couple, the so-called ligand (L) orbitals.[25] The reduction of the Hilbert space by use of ligand orbitals is crucial for efficient MLFT calculations as is explained in more detail in Appendix D. For each TM d orbital there is exactly one such linear combination. The right-hand panel of Fig. 4 shows the five Ni d orbitals together with the five Ni-centered L orbitals of the same symmetry. There is an important difference between the L t_{2g} and L e_g orbitals: Whereas the L t_{2g} orbitals are bonding (the same color) between nearest O p Wannier orbitals, and thus give rise to a substantial O-O σ-like bond charge, the L e_g orbitals are antibonding (different colors). As a result, the energies of the L t_{2g} and e_g orbitals are respectively $T_{pp} = pp\sigma - pp\pi$ below and above ϵ_p.[64,65]

We finally complete the level diagram by including the covalent hopping integrals $V_{t_{2g}} = pd\pi \times 4/\sqrt{4} = 2pd\pi$ and $V_{e_g} = -\frac{\sqrt{3}}{2} pd\sigma \times 4/\sqrt{4} = -\sqrt{3}pd\sigma \sim 3pd\pi$ (Ref. 66) between the L p and TM d orbitals of, respectively, t_{2g} and e_g symmetry. The t_{2g} hopping gives rise to an L p-like π and a TM d-like π^* level, and the e_g hopping gives rise to an L p-like σ and a TM d-like σ^* level. It is these π^* and σ^* levels which in the solid broaden into Ni t_{2g} and e_g bands. The σ^* level is close to the Fermi level in the LDA and this indicates that the σ^* orbital is half full. The π, σ, and π^* orbitals have considerably lower energies and are fully occupied.

Our MLFT calculations include Coulomb correlations beyond the one-electron mean-field potentials discussed so far, but only among the TM d orbitals. Arguments for treating the L p orbitals as well as their Coulomb repulsion with the TM d orbitals at the LDA level are that the L p orbitals are fairly delocalized and that they are almost fully occupied. As an example, we can safely neglect correlation in an event where two holes meet on a single oxygen atom and scatter. The Coulomb correlations are responsible for the multiplet structure, and we keep them among the Ni d orbitals, but make a distinction between the spherical (U, Δ) and the nonspherical repulsions.

The spherical part of the Coulomb repulsion, often parametrized by U, is strongly screened in a solid. If a Ni d electron is removed, there will be a charge flow into the Ni $4s$ orbital, for example, which reduces the energy cost of such an excitation. Although several calculations of the screened U have been presented in the past,[44,67–77] we fit U such as to obtain the best agreement between our MLFT calculation and the experimental multiplet spectra.[78,79] The parameter Δ is the orbitally averaged (spherical) part of the difference between the on-site energies of the Ni d orbitals and the L p orbitals at a filling of eight electrons in the Ni d shell. In the LDA, as well as for the ground state found in our MLFT calculations, the Ni d occupation exceeds 8 due to the covalency with the oxygens. The relation between Δ, as defined in MLFT calculations, and $\epsilon_d - \epsilon_p$, as obtained from the LDA, is rather nontrivial and we shall therefore treat, not only U, but also Δ as an adjustable parameter. In the foreseeable future, it should be possible to calculate U and Δ from first principles.

The nonspherical parts of the Coulomb interactions we can easily calculate because the multipole interactions between two d electrons are hardly screened. For example, the Coulomb repulsion between two $d_{x^2-y^2}$ electrons is obviously larger than that between a $d_{x^2-y^2}$ electron and a d_{3z^2-1} electron, but to screen this difference requires electrons with high angular momentum around the Ni site; a Ni 4s electron, for instance, could not do it. Also electrons on neighboring sites are inefficient in screening the multipole because it decays fast ($\propto r^{-k-1}$). It has been shown that neglecting any screening of the multipole part of the Coulomb interaction gives reasonable agreement between theory and experiment.[80] Also in the present work, we shall neglect any screening of the multipole part of the Coulomb interaction and shall find reasonable agreement with experiments.

Multipole interactions are the cause of the Hund's-rule energy. For example, two $d_{x^2-y^2}$ electrons must have different spins, whereas two electrons in different d orbitals, and hence less repulsive, may be in a spin-triplet state, as well as in the spin-singlet state. Experimentally it has been shown[80] that the multipole interactions of the Coulomb interaction, are reasonably well approximated by assuming that the d orbitals have the pure-angular-momentum form: $R(r)\,Y_{2m}(\hat{\mathbf{r}})$. The inset in Fig. 3 is a table of the values of the Slater integrals obtained using the Ni^{2+} ionic radial function $R(r)$, as well as the radial functions obtained by averaging the Ni t_{2g} and e_g Wannier orbitals over solid angles. The Slater integrals for d orbitals are

$$F^{(k)} = \int\int \frac{r_<^k}{r_>^{k+1}} R^2(r_1) R^2(r_2)\, r_1^2 dr_1\, r_2^2 dr_2, \qquad (1)$$

where $r_< = \min(r_1,r_2)$, $r_> = \max(r_1,r_2)$, and $k = 0$, 2, or 4. The definitions of U and the Hund's-rule exchange J_H vary: The average repulsion between two d orbitals is $U_{\text{av}} = F^{(0)} - \frac{14}{441}(F^{(2)} + F^{(4)})$. However, in order to discuss the Mott gap, one uses the energy difference between the lowest multiplets of different configurations and that has led to the definition $U = F^{(0)} + \frac{4}{49}F^{(2)} + \frac{36}{441}F^{(4)}$. The Hund's-rule exchange can be defined either as $J_H = \frac{1}{14}(F^{(2)} + F^{(4)})$ or as $J_H = \frac{2.5}{49}F^{(2)} + \frac{22.5}{441}F^{(4)}$. The bare $F^{(0)}$ as calculated from the Wannier orbitals is of the order of $\sim$25 eV. This is clearly much too large because the monopole part of the Coulomb repulsion is strongly screened. The values of $F^{(2)}$ and $F^{(4)}$ are respectively $\sim$11 and $\sim$7 eV, in good agreement with experimental values, as we shall see. The multiplet interactions are quite large and lead to a multiplet splitting of the Ni d^8 configuration of about 7.5 eV, which is the energy difference between the ^3F ground-state configuration and the highest excited singlet of ^1S character. This is larger than the Ni d bandwidth and therefore not a small energy.

We will compare our results to several experiments, including core-level spectroscopy. Once a core hole is made, the interaction between the core and valence electrons becomes important. Here again we will make a distinction between the multi- and monopole interactions. The monopole interactions $U_{2p,3d}$ and $U_{3p,3d}$ will, as for the valence states, be taken from fits to experiment.[78,79] For the multipole interactions, i.e., the Slater integrals $F^2_{p,d}$, $G^1_{p,d}$, and $G^3_{p,d}$, we again assume that screening can be neglected, which allows us to directly calculate these integrals from the core and valence Wannier orbitals. The core Wannier orbitals are equivalent to atomic wave functions since they have no intersite overlap. It is important to use a scalar-relativistic method for the calculation, as well as to calculate the core wave functions for the final state occupations, which requires an open-shell calculation. We used an atomic Hartree-Fock code to obtain these core wave functions,[61] but any open-shell, scalar-relativistic method should give similar results. Specific values of the Slater integrals can be found in Table I in Appendix C.

We now have all ingredients needed to perform MLFT calculations of experimentally observable quantities. But before we do this, we will introduce similar ligand-field calculations for MnO and SrTiO$_3$. This allows us to compare oxides of early, intermediate, and late transition metals and show that the method is likely to apply to a range of correlated transition-metal compounds.

III. NiO, MnO, AND SrTiO$_3$

In Fig. 5 we show from top to bottom the LDA band structures of NiO, MnO, and SrTiO$_3$ calculated in the same way as in Fig. 2 and explained in the previous section, with details given in Appendix C. Whereas NiO and MnO have the fcc rocksalt structure, SrTiO$_3$ has the simple-cubic (sc) perovskite structure in which the Sr cube has Ti at its body center and O at its face centers; in MLFT we treat the TiO$_6$ cluster. Going from NiO to MnO, the TM-electron and -proton counts are both reduced by 3, whereby the d-band filling gets reduced from d^8 to d^5. Concomitantly, we see that the 3d bands move up in energy relatively to the 4s and O 2p bands, by about 1.5 eV. The p and e$_g$ bandwidths as well as the e$_g$-t$_{2g}$ splitting decrease, presumably due to the increased ionicity, $\epsilon_d - \epsilon_p$. Going finally to SrTiO$_3$, the TM-electron and -proton counts are further reduced by 3, but due to the change of stoichiometry, the nominal d-band filling is now reduced to d^0 rather than to d^2. SrTiO$_3$ is a band insulator and the LDA band structure shown in the bottom panel agrees with the ionic configuration Sr^{2+}Ti^{4+}(O^{2-})$_3$: We see nine full O 2p bands separated by a 2 eV gap from the three empty Ti 3d(t$_{2g}$) bands. The latter are separated by a small gap from the two Ti 3d(e$_g$) bands which overlap the two Sr 4d(e$_g$) bands and the bottom of the Ti 4s band. The three Sr 4d(t$_{2g}$) bands are pushed up in energy by covalent $pd\sigma$ interaction with the 12 nearest oxygen neighbors[50] and thus lie more than 8 eV above the Fermi level. Due to the different structure and stoichiometry of SrTiO$_3$, its bands are quite different from those of NiO and MnO.

The agreement between the O p-like and TM d-like bands obtained with the LAPW method and those obtained with the minimal basis set of NMTOs is almost perfect for NiO and MnO. The agreement is also satisfactory for SrTiO$_3$, although

TABLE I. Top panel: MLFT parameters obtained from LDA. The Slater integrals are obtained from the spherically averaged Wannier orbitals. Lower two panels: One-electron tight-binding parameters as obtained from the LDA TM *d* O *p* Wannier-orbital set. The hopping is from the first to the second orbital displaced by the vector [*abc*]. [000] denote on-site energies. Shown are only those values larger than 10 meV. The bold numbers enter in the MLFT calculations; the normal font longer-range hopping integrals are truncated in the cluster approximation. For the *p*-*p* hopping in the [001] direction of $SrTiO_3$ the first two values listed concern hopping along an O-Ti-O bond. The last three values concern O-O hopping in the Sr-O plane. The notation for the e_g orbitals is such that $d_{z^2} \equiv d_{3z^2-1}$ and $d_{\mathsf{XY}} \equiv d_{x^2-y^2}$. All values are in eV.

	V_{e_g}	$V_{t_{2g}}$	$10Dq$	T_{pp}	ζ_{3d}	$F^{(2)}_{dd}$	$F^{(4)}_{dd}$	ζ_{2p}	$F^{(2)}_{2p3d}$	$G^{(1)}_{2p3d}$	$G^{(3)}_{2p3d}$	ζ_{3p}	$F^{(2)}_{3p3d}$	$G^{(1)}_{3p3d}$	$G^{(3)}_{3p3d}$	
NiO	2.06	1.21	0.56	0.72	0.08	11.14	6.87	11.51	6.67	4.92	2.80	1.40	12.87	15.89	9.58	
MnO	1.92	1.15	0.67	0.53	0.04	9.35	5.78	6.85	5.29	3.77	2.14	0.77	10.93	13.56	8.15	
$SrTiO_3$	4.03	2.35	1.79	0.99	0.02	8.38	5.25	3.78	4.23	2.81	1.59	0.43	9.85	12.08	7.35	
	$[00\frac{1}{2}]$						$[\frac{1}{2}\frac{1}{2}0]$							$[\frac{1}{2}\frac{1}{2}\frac{1}{2}]$		
	$d_{z^2}p_z$	$d_{xz}p_x$	p_xp_y	p_yp_x	p_xp_x	p_zp_z	$d_{z^2}d_{z^2}$	$d_{\mathsf{XY}}d_{\mathsf{XY}}$	$d_{xy}d_{xy}$	$d_{xz}d_{xz}$	$d_{xz}d_{yz}$	$d_{xy}d_{z^2}$	$d_{xy}p_y$	$d_{xy}p_z$	$d_{z^2}p_z$	
NiO	**1.19**	**−0.60**	**0.38**	**0.38**	**0.25**	−0.10	−0.01	−0.08	−0.20	0.06	0.04	0.04	−0.03	−0.02	0.00	
MnO	**1.11**	**−0.57**	**0.28**	**0.28**	**0.19**	−0.09	−0.04	−0.06	−0.26	0.08	0.05	0.04	−0.03	−0.02	0.02	
$SrTiO_3$	**2.33**	**−1.18**	**0.42**	**0.34**	**0.24**	−0.07	—	—	—	—	—	—	—	—	—	
				[001]						$[0\frac{1}{2}1]$			$[11\frac{1}{2}]$		[000]	
	p_zp_z	p_xp_x	p_zp_z	p_xp_x	p_yp_y	$d_{z^2}d_{z^2}$	$d_{xz}d_{xz}$	$d_{xy}p_x$	$d_{yz}p_z$	$d_{z^2}p_y$	$d_{z^2}p_z$	$d_{xz}p_x$	$d_{xz}p_y$	$d_{xy}p_x$	ϵ_p	ϵ_d
NiO	0.02	−0.04	—	—	—	−0.01	−0.03	0.00	0.02	−0.03	0.00	0.00	0.00	0.00	−4.75	−1.35
MnO	0.05	−0.03	—	—	—	−0.06	−0.05	0.00	0.02	−0.03	−0.01	0.00	0.00	0.00	−5.22	−0.39
$SrTiO_3$	−0.01	−0.11	0.06	−0.02	−0.02	0.05	−0.13	−0.02	0.05	−0.03	0.00	−0.02	−0.01	−0.02	−1.53	3.31

near the bottom of the Ti t_{2g} band, and at various places in the O 2p band, small discrepancies may be detected. These are most likely due to the OMTA causing a slightly inaccurate description of the hybridization with the high-lying Sr 4*d* and Ti 4*s* bands.

From the right-hand side of the figure, we see that for all three materials the TM 3*d* Wannier orbitals are very well localized. This is a necessary condition for using them in MLFT. We do not show the O 2*p* orbitals as in Fig. 2, but had we done so for $SrTiO_3$, we would have seen not only bonding Ti 4*s* character of the *p* orbital pointing toward Ti, but also bits of bonding Sr 4*d* and 5*s* characters of the two other *p* orbitals, which point toward Sr.[50] The good localization of the Ti e_g orbitals is related to the feature seen in the left-hand panel around 8 eV, that the *N*MTO Ti e_g band interpolates *smoothly* across the avoided crossing of the LAPW Ti e_g and Sr e_g bands. Had this not been the case, the Ti e_g Wannier orbitals would have been long ranged. Hence, we can construct a minimal set of *localized N*MTOs, even when bands described by the set are crossed by and hybridize with other bands, provided that we can choose the $N+1$ expansion energies outside the range of those other bands. For $SrTiO_3$, we used $\epsilon_0 = -2.6$ and $\epsilon_1 = 1.5$ eV.

The 3*d* Wannier orbitals for the three oxides are very similar; they merely contract along the 3*d* row of the periodic table. This is seen when going from the bottom to the top in the right-hand panel of Fig. 5, and even more clearly in Fig. 6 where we show the angular-averaged t_{2g} Wannier orbitals. The well-known reason for this orbital contraction is as follows: Upon proceeding one step along the TM row, a proton and an electron are added. The electron incompletely screens the attractive potential from the proton seen by another valence electron, and as a result, the one-electron potential becomes deeper and deeper upon proceeding along the series, until the *d* shell is full and the screening is complete. Since this mechanism is atomic, the shapes of our 3*d* Wannier functions are fairly robust and the chemistry merely changes tails—and thereby normalizations—a little. This is what we saw in Fig. 3. For that reason, the contraction seen in Fig. 6 of the t_{2g} radial functions—which are less influenced by O than the e_g functions—closely follows that of the 2+ ionic radii, which are 0.72 (Ni^{2+}), 0.80 (Mn^{2+}), and 0.90 Å (Ti^{2+}), in the sense that at the respective radius, all three radial functions have about the same amplitude. This happens although the Wannier orbitals are calculated for the real solids, which in the case of $SrTiO_3$ have a Ti-O distance far smaller than expected from the size of the Ti t_{2g} function in Fig. 6. That the chemical binding of $SrTiO_3$ is different than those of NiO and MnO also becomes clear by adding the accepted ionic radius of O^{2-} (1.40 Å) to the M^{2+} radii given above (*M* represents the transition metal), obtaining 2.12, 2.20, and 2.30 Å for the *M*-O distance in, respectively, NiO, MnO, and $SrTiO_3$. The real distances in NiO and MnO are nearly the same, but much smaller (1.95 Å) in $SrTiO_3$.

The short Ti-O distance is of course reproduced by using the Ti^{4+} radius of 0.68 Å which corresponds to the band-structure configuration $Sr^{2+}Ti^{4+}(O^{2-})_3 = \mathrm{Sr}\,4d^0\ \mathrm{Ti}\,3d^0\,(\mathrm{O}\,2p^6)_3$. This ionic picture of the binding seems to neglect the Ti-O and Sr-O covalencies predicted by the LDA, i.e., the fact that there is a considerable amount of Ti 3*d* and Sr 4*d* partial-wave character in the O 2*p* bands. But this is only apparently so: The Ti 3*d* and Sr 4*d* radial functions are essentially exponentially increasing because they solve the respective radial Schrödinger equation for O 2p-band energies, which are far below those of the Ti 3d and Sr 4d bands. Hence, these partial waves simply complete the shape of the O 2p Wannier orbitals inside the Ti and Sr MT spheres.

IV. COMPARISON WITH EXPERIMENTS

In order to test the quality of MLFT calculations using the LDA Wannier orbitals, we now present a comparison between

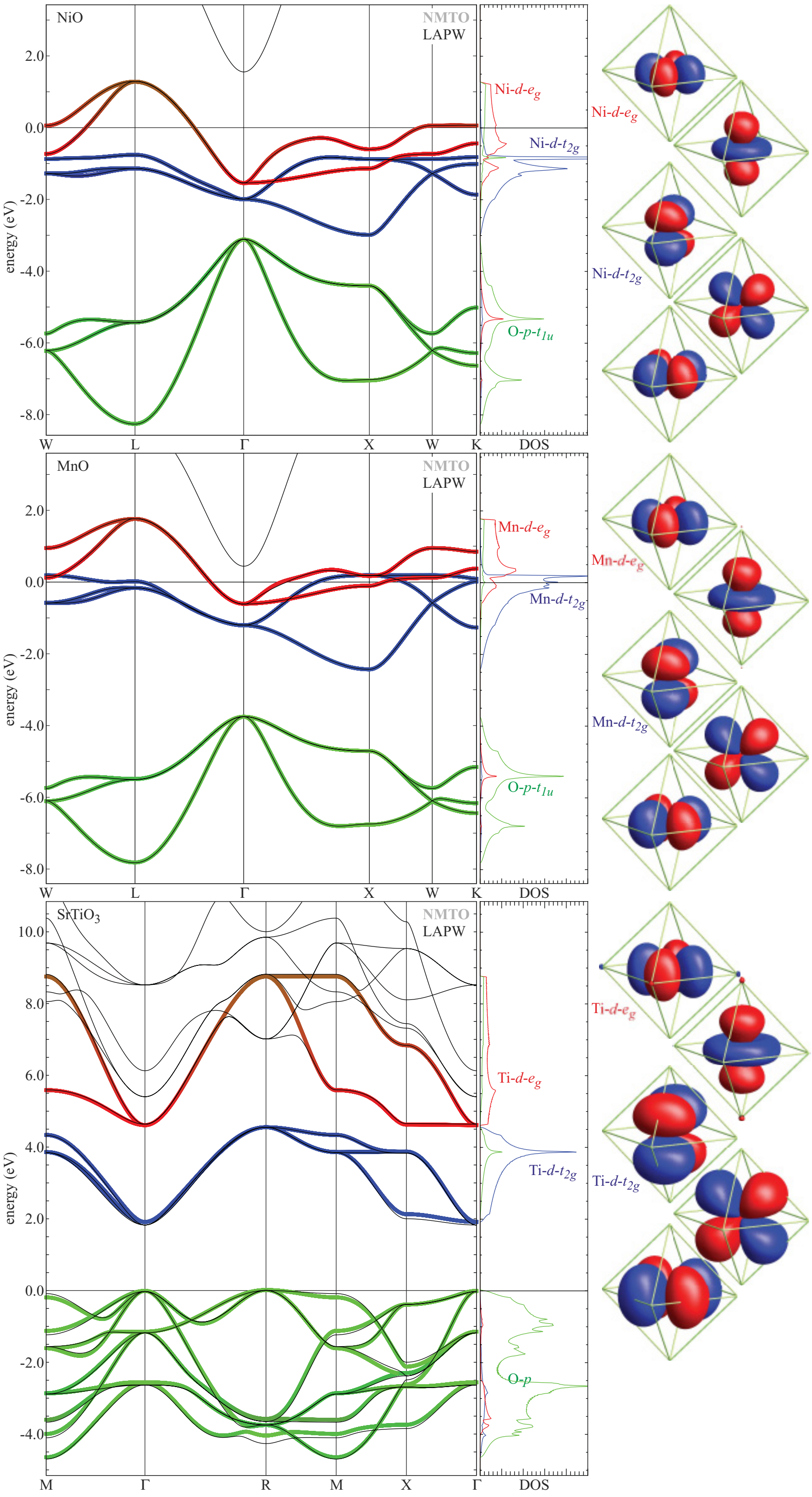

FIG. 5. (Color online) As Fig. 2, but for fcc NiO (d^8), fcc MnO (d^5), and sc $SrTiO_3$ (d^0). On the right-hand side, the oxygen orbitals are not shown.

theory and experiment for several established spectroscopies, which show TM excitons. Such locally bound states are represented well within the small cluster used in the MLFT. The materials considered, namely, NiO, MnO, and $SrTiO_3$, are insulators, thus justifying the theoretical methodology further. NiO, MnO, and $SrTiO_3$ have local ground states which are well understood, and the spectra shown here have already been explained in the literature. Different in the present paper is that the MLFT parameters (except for U and Δ) are not fitted to the experiment, but calculated *ab initio*.

In the following subsections we first discuss x-ray absorption at the $L_{2,3}$ edge, which probes TM $2p$ to $3d$ excitations. Next we show TM $2p$ core-level x-ray photoemission experiments on an impurity system. Both $2p$ XAS and $2p$ XPS excite the same core states and the difference is that in x-ray absorption the electron is excited into the local $3d$

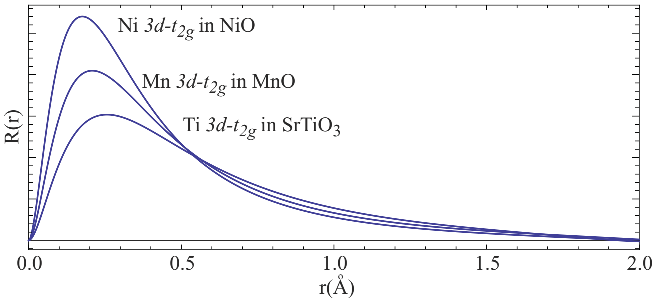

FIG. 6. (Color online) Angular-averaged TM t_{2g} Wannier orbitals in NiO, MnO, and SrTiO$_3$. The distance to oxygen is 2.09 Å in NiO, 2.21 Å in MnO, but only 1.95 Å in SrTiO$_3$.The ionic radii are 0.72 for Ni^{2+}, 0.80 for Mn^{2+}, 0.90 for Ti^{2+}, but only 0.68 Å for Ti^{4+}.

shell whereas photoemission excites the core electron into vacuum states. The resulting spectra are very different. We then continue with core excitations measured with inelastic x-ray scattering. From a theoretical point of view, inelastic x-ray scattering of core to valence excitations and x-ray absorption of core to valence excitations is very similar. The initial and final states probed are the same. The difference is that whereas x-ray absorption is mainly caused by dipole transitions, inelastic x-ray diffraction is caused by multipole transitions determined by the length of the transferred momentum. Finally, in the last subsection, we show inelastic x-ray scattering of d-d excitations in NiO. These spectra are particularly instructive as they allow for a relatively straightforward understanding of how the different interactions contribute to each multiplet excitation. For pedagogical reasons we provide a brief introduction to each of the experimental techniques. A more thorough description of these techniques can be found in textbooks, e.g., those by De Groot and Kotani,[81] Stöhr,[82] and Schülke.[83]

A. $L_{2,3}$ edge x-ray absorption

X-ray absorption spectroscopy at the TM $L_{2,3}$ edge is a technique whereby a TM $2p$ core electron is excited into the $3d$ valence shell. The excitation energy is in the x-ray range and varies from ∼440 eV for Ti to ∼855 eV for Ni. The excitations are dipole allowed, which make them so intense that spectra with very little noise can be obtained. The spectra split into two sets of peaks, the L_3 and L_2 edges, due to spin-orbit coupling in the TM $2p$ core hole. This results in a $2p_{j=3/2}$ level (L_3 edge) lying $\frac{3}{2}\zeta_{2p}$ above a $2p_{j=1/2}$ level (L_2 edge). For core levels the relativistic spin-orbit coupling is strong and element dependent: $\zeta_{2p} = 3.78$ eV for Ti, 6.85 eV for Mn, and 11.50 eV for Ni. Hence, in Fig. 7 we see the L_3 and L_2 edges at 640 and 650 eV for MnO, and at 852 and 870 eV for NiO.

For SrTiO$_3$, $\frac{3}{2}\zeta_{2p}$ is of similar size as the $2p$-$3d$ multiplet splitting, i.e., the L_2 and L_3 edges overlap. The splitting within an L_2 or L_3 edge is due to the combined interaction of covalent ligand-field effects and Coulomb interactions between the $3d$ electrons and between the $2p$ core hole and the $3d$ electrons. This leads to the relatively involved spectra with many features as seen in Fig. 7. Even for SrTiO$_3$ where one might be tempted to relate the four intense peaks in the $2p$ XAS spectrum to excitations from the $2p_{j=3/2}$ or $2p_{j=1/2}$ orbitals into either the t_{2g} or the e_g orbitals, the intensity ratios 4:2 between excitations from respectively $2p_{j=3/2}$ and $2p_{j=1/2}$ core holes, and 3:2 between excitations to respectively t_{2g} and e_g states) do not follow this one-electron picture: Assigning the peaks at 458, 460, 463, and 465 eV to excitations of the form $2p_{j=3/2} \rightarrow t_{2g}$, $2p_{j=3/2} \rightarrow e_g$, $2p_{j=1/2} \rightarrow t_{2g}$, and $2p_{j=1/2} \rightarrow e_g$, respectively, would yield the intensity ratios 12:8:6:4, which are clearly not observed. On the other hand, starting from a $2p^5 3d^1$ final-state configuration in a cubic crystal field does yield the correct intensities,[88] plus several small peaks. Our *ab initio* results, shown in blue in the figure, confirm this interpretation. Within the atomic $2p^5 3d^1$ excitonic picture the interpretation in terms of t_{2g} and e_g excitations of the L_3 and L_2 edges for the four peaks might still be a reasonable starting point, but one should realize that there is a considerable mixing between states due to Coulomb interactions.

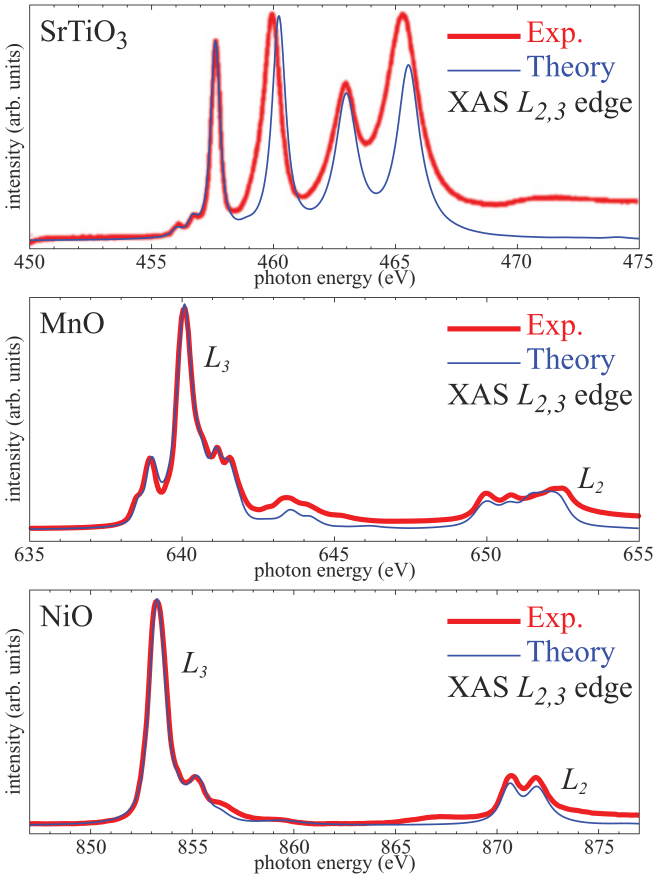

FIG. 7. (Color online) Comparison of the experimental (thick red) and MLFT (thin blue) TM $2p$ ($L_{2,3}$ edge) core-level x-ray absorption spectra for SrTiO$_3$, MnO, and NiO. The experimental SrTiO$_3$ spectra are reproduced from Uehara *et al.* (Ref. 84), the MnO spectra from Csiszar *et al.* (Refs. 85 and 86), and the NiO spectra from D. Alders *et al.* (Ref. 87).

The cluster eigenstates cannot be represented by single Slater determinants. For correlated TM compounds, the spectral line shape is governed by multiplet effects leading to involved spectral functions, not obviously related to the density of states.[89,90] The spectra are therefore generally used as fingerprints which contain unique features resembling the local ground-state properties. The energy of the final state is determined by local atomiclike physics. The intensity with which each state can be reached depends, via the optical selection rules, on the ground-state symmetry and the polarization of the light. This can lead to large spectral changes for small changes in the ground state.[81,89,90] For example, a p electron can only be excited into an $d_{x^2-y^2}$ orbital with x- or y-polarized light, but not with z-polarized light. Changing the orbital occupation can therefore lead to a strong polarization dependence which for certain multiplets can be as strong as 100%.[91] Due to the strong TM $2p$ spin-orbit coupling, the XAS spectra are also sensitive to the spin of the ground-state.[92,93]

Theoretically, as well as experimentally, one finds that the monopole part of the $2p$-$3d$ Coulomb interaction is larger than that of the $3d$-$3d$ interaction.[61,78,79] This leads to strongly bound excitons at the TM $L_{2,3}$ edge and allows one to describe the spectra using MLFT. Besides these excitonic states, excitations into nonbound states are also possible.[94] Such excitations essentially probe the conduction bands of the compound. For NiO both excitations are clearly visible in the experimental spectra shown in the bottom panel of Fig. 7: The excitonic bound states give rise to sharp excitations which extend upward from 852 eV; they are seen to agree very well with our MLFT spectra. At 865 eV the experimental NiO spectra show an *edge jump* where the cross section for photon absorption increases discontinuously. This is the onset of L_3 excitations into the conduction-band continuum without formation of bound states. These continuum excitations are of course not reproduced with MLFT. The L_2 excitations into bound excitons give rise to the sharp features starting at 870 eV and captured by our MLFT. Around 856 eV there is a slight disagreement between the theoretical and experimental Ni L_3 edge spectra which might be due to the neglect of the Ni $4s$ orbitals in our cluster basis set.

Looking at NiO, MnO, and $SrTiO_3$, one may notice that our calculations reproduce the low-energy parts of the spectra better than the high-energy parts. The former are most excitonic and therefore best described by the small basis set in the cluster. It may furthermore be noticed that not only are the edge jumps absent in the calculation, but also the interference between the excitonic excitations of the L_2 edge and the continuum states of the L_3 edge. These interference effects give rise to Fano-like line shapes present in the experiment, but not in the theory. The effect is relative small as the interference between $2p_{j=3/2}$ and $2p_{j=1/2}$ states is forbidden in many channels. There is, however, a substantial mixing of core states due to Coulomb interactions, which could be the main reason for the interference effects between continuum and excitonic states of the L_3 and L_2 edges.

Nevertheless, the agreement between MLFT and experiment is rather good in Fig. 7 for all three TM oxides. This agreement is as good as—or even better than—that obtained for calculations in which all standard MLFT parameters are optimized to give the best fit to experiment.[81,84–87] There are many parameters in such a calculation and finding the best fit is not trivial. The use of *ab initio* values for an otherwise equivalent MLFT calculation can therefore be of great help to interpret x-ray absorption spectra and thus also in the understanding of elastic resonant x-ray diffraction (RXD) spectra,[95] and the resonant energy dependence of resonant inelastic x-ray scattering (RIXS).[96,97] For systems with lower local symmetry, the number of parameters is even larger, and so is the need for values determined *ab initio*.

Compared with other *ab initio* methods used for the calculation of the $L_{2,3}$ edges of correlated transition-metal compounds,[32–37,98–100] the current method preforms well. For d^0 compounds, i.e., band insulators like $SrTiO_3$, very powerful methods based on multiple-scattering formalisms[98,99] or the Bethe-Salpeter equations[100] are available. For Mott-Hubbard or charge-transfer insulators, *ab initio* configuration-interaction calculations of high quality have been performed for finite-sized clusters.[32–37] Our MLFT method has the advantage that its one-electron basis functions exactly describe the relevant bands for the infinite crystal and at the same time localize so well that one can afford to include correlations beyond the LDA for merely the TM d orbitals. This allows for very efficient, but still accurate, many-body calculations in the framework of the well-studied multiplet ligand-field theory.

B. $2p$ core-level photoemission of $Ni_{0.03}Mg_{0.97}O$

Core-level photoemission is uninteresting from a one-electron point of view. Core levels are atomiclike and have no momentum-dependent dispersions and therefore δ-peaked densities of states. Accordingly, $2p$ photoemission is expected to yield two spin-orbit-split peaks with intensity ratio 2:1. However, the experimental spectra[101] from Ni $2p$ core-level photoemission in $Ni_{0.03}Mg_{0.97}O$ exhibit four distinct spectral features, as shown in Fig. 8. Emission from the Ni $2p_{3/2}$ level gives rise to the structure between 852 and 868 eV and emission from the $2p_{1/2}$ level to the structure between 870 and 886 eV. The structure between 860 and 868 eV originates from multiplet excitations with main character $\underline{2p}_{3/2}3d^8$ (with the underbar indicating a hole) while the peak centered at 855 eV belongs to an excitation with main final-state character $\underline{2p}_{3/2}3d^9\underline{L}$. It is the strong Coulomb attraction between the $2p$ core hole and the $3d$ electron which causes the latter state to have lower energy than the former, and thus screens the core hole by driving charge in from the ligand. Between 870 and 886 eV, this spectrum of screened and unscreened states is repeated, but now for excitations from the $2p_{1/2}$ core level. Our MLFT spectra agree well with the experimental spectra[101] and with MLFT calculations for Ni impurities in MgO with fitted parameters.[101] The resulting interpretations of the experiment are the same.

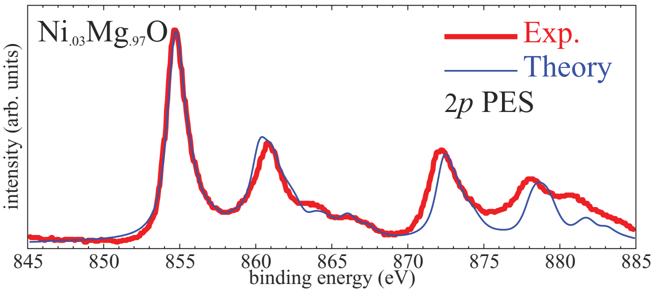

FIG. 8. (Color online) Comparison of the experimental (thick red) and MLFT (thin blue) Ni $2p$ core-level photoemission spectra of NiO in the impurity limit. The experimental spectra are reproduced from Altieri *et al.* (Ref. 101).

These Ni $2p$ core-level photoemission spectra are strikingly different from the previously considered Ni $2p$ x-ray absorption spectra in the bottom panel of Fig. 7.[94] In core-level x-ray absorption, a TM core electron is excited into the $3d$ shell of the same atom, whereby the sample remains locally neutral. The $3d$ electron can bind with the core hole left behind and thereby screen the core-hole potential. This gives rise to the strong excitonic peaks seen in the x-ray absorption spectrum. In core-level photoemission, a core electron is emitted from the sample (excited into the vacuum) and can therefore not screen the core hole left behind. The core hole is either screened by the surrounding ligands or left unscreened, which gives rise to higher-energy excitations.

Photoemission spectra are generally not excitonic. It might therefore seem strange to use MLFT to calculate those spectra. Nevertheless, experience has shown that many features of photoemission from correlated transition-metal compounds can be captured by full multiplet theory for a local cluster. Photoemission combined with cluster calculations has contributed greatly to our understanding of correlated TM and rare-earth compounds.[64,78] The influence of nonlocal screening, i.e., the effect of the material being a solid and not a single impurity, has been studied experimentally by comparing the core-level photoemission from TM impurities with that from the TM compounds.[101] The main features of the Ni $2p$ photoemission spectra from $\mathrm{Ni_{0.03}Mg_{0.97}O}$ are the same as from NiO. The largest bulk effect is a splitting of the peaks at 855 and 873 eV.

Important progress in understanding bulk valence photoemission from NiO has been made recently by solving the LDA O p Ni d Wannier-orbital Hubbard model in the dynamical mean-field approximation[102,103] (LDA + DMFT) and also by using the variational cluster approximation.[104] How important correlation between different Ni sites is, and therefore how important the inclusion of dynamical nonlocal screening effects is,[105] remains an open question. On a different level, MLFT is able to reproduce a substantial part of the photoemission spectra, even though these are not excitonic.

C. Nonresonant inelastic x-ray scattering at the $M_{2,3}$ edge

In Sec. IV A, we compared experiments and MLFT for core-level x-ray absorption. Now we shall discuss core-level spectra obtained with a technique which from a theoretical point of view is very similar to x-ray absorption, namely, inelastic x-ray scattering. In XAS at the TM $M_{2,3}$ edge, a TM $3p$ core state is excited to a $3d$ conduction state by absorption of a photon. The same excitation can be caused when a photon is scattered inelastically and only part of its energy is absorbed.[83,106–108] The major difference between XAS and IXS is that, for the former, the energy of the photon has to equal the absorption edge, whereas for the latter, the energy of the photon should be (much) higher than the absorption edge since only a fraction of its energy is absorbed. For XAS at the TM $M_{2,3}$ edge, the leading interaction is of dipole character, i.e., one can use the long-wavelength limit. For IXS, the transferred momentum can be selected by looking at different scattering angles and energies: for small momentum transfers, dipole transitions are measured, and for larger momentum transfers, octupole transitions.[107] In Fig. 9 we show the nonresonant IXS at the $M_{2,3}$ edge in MnO for high magnitude momentum transfers where octupole transitions are the strongest.

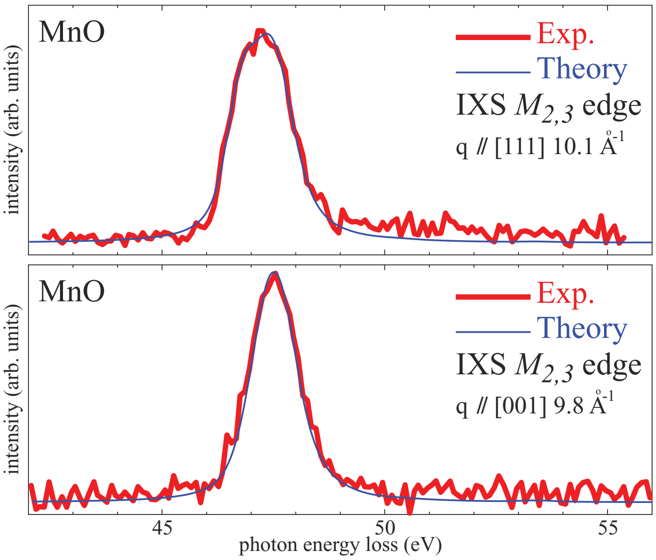

FIG. 9. (Color online) Comparison of the experimental (thick red) and theoretical (thin blue) Mn $3p$ ($M_{2,3}$ edge) nonresonant inelastic x-ray scattering spectra of MnO at large momentum transfer (**q**). The two panels give spectra for different directions of momentum transfer. They exhibit the generalized natural linear dichroism present for an octupole transition in cubic symmetry. The experimental spectra are reproduced from Gordon *et al.* (Ref. 109).

There is a clear difference between the $L_{2,3}$ ($2p$ to $3d$) and $M_{2,3}$ ($3p$ to $3d$) edges in MnO. One reason is that the spin-orbit coupling constant for $3p$ is much smaller than for $2p$, e.g., for Mn, $\zeta_{2p} = 6.85$ and $\zeta_{3p} = 0.77$ eV. The splitting between the M_3 and M_2 edges is thus much smaller (not resolved in the experimental spectra) than the splitting between the L_3 and L_2 edges. Another reason why the $L_{2,3}$ and the $M_{2,3}$ edges look different comes from the fact that the $3p$ wave function is larger than the $2p$ wave function due to the extra node. This leads to a smaller monopole part of the Coulomb repulsion and larger multipole interactions between the p and $3d$ orbitals. In general, for excitations within the same radial shell the multiplet splittings are larger than the excitonic binding energy.[110] This has important consequences. The highest-energy multiplets of the $M_{2,3}$ excitations are pushed above the continuum edge and form broad resonances instead of sharp mulitplets. The low-energy multiplets, on the other hand, are still sharp excitonic states. Due to the strict selection rules applicable to XAS and IXS, one can choose the experimental geometry such that only particular excitations are allowed. The spectra shown in Fig. 9 are octupole dominated and sensitive only to the low-energy excitonic features in the spectra. One would not be able to reproduce the broad dipole resonances with MLFT.

One of the beauties of octupole transitions is that they show dichroism in cubic symmetry.[109] This can be seen in the two different panels of Fig. 9, and is well reproduced by our theory. For a dipole transition one cannot distinguish cubic from spherical symmetry. [A transition of angular momentum $L = 1$ branches to a single irreducible representation (T_{1u}) in cubic symmetry.] An octupole transition, however, shows nice dichroism in cubic symmetry, whereby the momentum transfer **q** for IXS takes the place of the light polarization ϵ in XAS. A transition of angular momentum $L = 3$ branches to three different irreducible representations in cubic symmetry, namely, T_{1u}, T_{2u}, and A_{2u}. As a consequence, the dichroic spectra can be used to obtain detailed information about the differences in bonding of t_{2g} and e_g electrons. The shift in the spectral energy and the change in spectral weight for excitations with **q** either in the [111] (top panel) or [001] (bottom panel) direction is related to the different energy of the t_{2g} and e_g electrons and the difference in occupation of these orbitals due to covalent bonding.

D. Nonresonant inelastic x-ray scattering of *d-d* excitations

This last section in which we compare MLFT with experiment deals with low-energy excitations without a core hole. It has recently been shown that surprisingly strong *d-d* or crystal-field excitations can be observed in NiO with nonresonant IXS for large momentum transfers.[111–113] These spectra contain similar information as the weak *d-d* excitations inside the optical gap observed with optical spectroscopy.[56,57] The difference between IXS and optics is that with optics these transitions, being even in parity, are forbidden and only become allowed by simultaneous excitation of a phonon and a crystal-field excitation. This makes a quantitative interpretation of optical *d-d* excitations involved. The interpretation of the nonresonant IXS is, on the other hand, straightforward and allows for a quantitative comparison.[107,114]

In Fig. 10 we show the experimental[112] and theoretical nonresonant IXS spectra for a powder of NiO at large momentum transfer (averaged over a transfer of 7.3–8.0 Å^{-1}). These spectra are governed by quadrupole and hexadecapole transitions between the 3*d* orbitals. The nonresonant IXS excitations are spin conserving. Locally the Ni ground-state configuration is d^8 with the t_{2g} orbitals fully occupied and the e_g orbitals half filled with $\langle S^2 \rangle = 2$, i.e., $S = 1$. In the one-electron picture, one can make a single excitation going from the t_{2g} shell to the e_g shell, which has an experimental energy of about 1.1 eV. This is the peak of T_{2g} final state symmetry in the experiment. In principle one could also excite two t_{2g} electrons simultaneously into the e_g subshell. This would give rise to a single peak at twice the energy. In a pure one-electron picture the double excitation is forbidden because nonresonant IXS couples a single photon to a single electron. Using full multiplet theory, however, both excitations have a finite intensity. This has to do with the strong t_{2g}-e_g multiplet interaction which mixes, for the excited states, the single Slater determinants. One even finds three peaks instead of two. The first peak indeed corresponds to an excitation of a single t_{2g} electron into the e_g subshell. The second peak is roughly the simultaneous excitation of two t_{2g} electrons into the e_g subshell. Finally, in order to understand the third peak, one should realize that the t_{2g} (xy) electron is Coulomb repelled more from an e_g $(x^2 - y^2)$ electron than from an e_g $(3z^2 - 1)$ electron because of the larger overlap of densities. This leads to multiplet splitting of the $t_{2g}^5 e_g^3$ states and to mixing of $t_{2g}^5 e_g^3$ and $t_{2g}^4 e_g^4$ states.

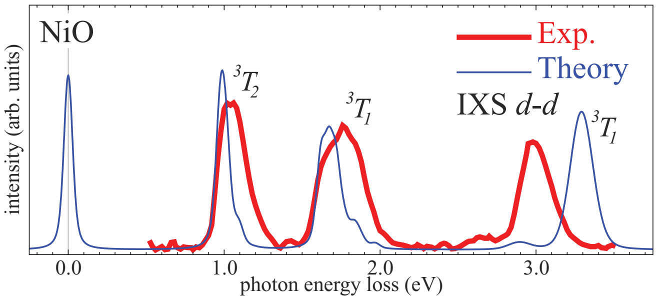

FIG. 10. (Color online) Comparison of the experimental (thick red) and MLFT (thin blue) nonresonant inelastic x-ray scattering intensity of low-energy *d-d* excitations. The experimental spectra are reproduced from Verbeni *et al.* (Ref. 112).

One could also have understood the energy and number of excitations by starting from spherical symmetry where Coulomb repulsion splits the $S = 1$ states into a lowest state of ^3F symmetry and an excited state of ^3P symmetry. In cubic symmetry the ^3F states branch into a $^3A_2$ ground state, a $^3T_2$ first excited state, and a $^3T_1$ second excited state. The ^3P state branches to a state of $^3T_1$ symmetry, which can mix with the highest excited state branching from the ^3F state. Such multiplet effects are hard to capture at the DFT level. Recent time-dependent DFT calculations with the LDA + U functional do show Frenkel excitons (*d-d* excitations) within the optical gap, but they cannot reproduce the correct number of multiplet states.[115]

Let us finally have a closer look at the comparison between the experimental and MLFT crystal-field excitations in NiO. MLFT gets the lowest excitation ($^3T_2$)5% too low and the highest ($^3T_1$)10% too high. As the $^3T_2$ energy is mainly determined by one-electron interactions, we conclude that the e_g-t_{2g} splitting due to covalency in our LDA-based calculation is 5% underestimated. At the same time, the multiplet splitting due to the Coulomb repulsion, i.e., the values of the $F_{dd}^{(2)}$ and $F_{dd}^{(4)}$ Slater integrals, are 10% overestimated. The latter could be a result of neglecting the screening of the multipole interactions, but not necessarily, because there are additional channels in which two 3*d* electrons can scatter into two higher excited states due to Coulomb repulsion. This gives rise to a multiplet-dependent screening, not easily described with a single screening parameter.[110]

V. CONCLUSIONS

We have shown how multiplet ligand-field theory calculations can be based on *ab initio* LDA solid-state calculations, in a similar way to that originally devised by Gunnarson *et al.*[43,44] and recently done for LDA + DMFT calculations. The resulting method could be named LDA + MLFT. The theory is very well suited for the calculation of local ground-state properties and excitonic spectra of correlated transition-metal and rare-earth compounds. Our TM *d* Wannier orbitals, which together with the O *p* Wannier orbitals span the LDA TM *d* and O *p* bands, are quite similar to atomic orbitals, and this justifies many previous studies using the latter.

We compared several experimental spectra (XAS, nonresonant IXS, photoemission spectroscopy) for $SrTiO_3$, MnO, and NiO with our *ab initio* multiplet ligand-field theory and found overall satisfactory agreement, indicating that our ligand-field parameters are correct to better than 10%. The covalency seems to be slightly underestimated and the Slater integrals for the higher multipole interactions overestimated. The method is expected to provide insights into the local properties of transition-metal compounds with only modest computational efforts.

ACKNOWLEDGMENTS

We would like to thank Eva Pavarini, Ove Jepsen, and Olle Gunnarsson for fruitful discussions. Support by the Deutsche Forschergemeinschaft through Grant No. FOR 1346 is gratefully acknowledged.

APPENDIX A: DEFINITION OF O AND TM ORBITALS, COVALENCY, AND FORMAL VALENCE

It is a general praxis to talk about Ni *d* and O *p* orbitals, even in a solid. The definition of local orbitals in a solid is not always clear. In this paper we choose such orbitals as generalized Wannier orbitals of a given local symmetry. For our materials, i.e., transition-metal oxides, there are two useful definitions for the Wannier orbitals, depending on the size of the basis set used and the energy bands they span. These two different definitions are often used in an ambivalent way. Here we explain the definitions of the two different sets of orbitals, by the example of NiO.

In Fig. 11 we show in the top row the Ni *d* and O *p* Wannier orbitals which are most atomiclike. Linear combinations of these eight orbitals span the eight bands shown on the left of the top row in Fig. 11. Due to covalency, the Ni *d* orbitals defined in this way are occupied by more than eight electrons. At the same time, the O *p* Wannier orbitals are occupied by fewer than six electrons, i.e., they have holes. When forming band states, the Ni *d* and O *p* orbitals mix and part of the O *p* character ends above the Fermi energy. One should not think of these extra electrons or holes as mobile charge carriers. These partial occupations are just a result of the choice of the basis set used, which is different from the eigenbasis, the band states.

A different choice of the Wannier orbitals, closer to the eigenfunctions, can be seen in the lower two rows of Fig. 11. Here we show from top to bottom the Ni d (e_g and t_{2g}) and O p t_{1u} orbitals. The Ni d orbitals are those five orbitals which together span the Ni d bands in the energy range from −3 to 2 eV. The O p orbitals are those three orbitals which together span the O p bands in the energy range from −8 to −3 eV.

In order to distinguish the two different sets of Wannier orbitals we have throughout this paper used italic font for the more localized atomiclike orbitals and roman font for the more extended orbitals. The difference in notation is quite subtle, but in almost all cases one can understand from the context which definition is meant.

The two basis sets of either atomiclike Ni *d* and O *p* orbitals or more delocalized Ni d and O p orbitals span the same bands and can thus be expressed in terms of linear combinations of each other. The unitary transformation between the two sets of Wannier orbitals is such that it diagonalizes the covalent interaction between the Ni *d* and O *p* orbitals. The Ni *d* and O *p* orbitals interact, whereas the Ni d and O p orbitals are noninteracting at the one-particle or LDA level. The five Ni d orbitals span the five d bands exactly and the three O p orbitals span the three O p bands exactly. The O p orbitals are bonding combinations of the TM *d* and O *p* orbitals. The TM d orbitals are antibonding combinations of the TM *d* and O *p* orbitals.

With the use of the Ni d (O p) Wannier orbitals, which span only the Ni d (O p) bands one can define the formal valence of Ni in NiO. It is common to state that O is 2−, i.e., has an occupation of p^6, and Ni is 2+, i.e., has an occupation of d^8. If one counts the electrons in the Wannier orbitals that separately span the Ni or O bands one immediately reproduces the formal valence. The occupation numbers are different if one looks at the more atomiclike Ni *d* and O *p* orbitals. For these orbitals covalence introduces holes in the O Wannier orbitals and extra electrons in the Ni Wannier orbitals. For the oxides described in the present paper, the occupations of the two kinds of Wannier orbitals are NiO $3d^8 \approx 2p^{5.4}3d^{8.6}$, MnO $3d^5 \approx 2p^{5.5}3d^{5.5}$, and SrTiO$_3$ $3d^0 \approx (2p^{5.7})_3 3d^{0.9}$.

Let us note that for our purposes, the Wannier d orbitals are not sufficiently localized. Nevertheless, in early LDA + DMFT calculations which could handle only a few correlated orbitals, even more "downfolded" t_{2g} or e_g Wannier orbitals [50,51] were used by necessity; they clearly exhibit the covalencies.[52]

APPENDIX B: COMPUTATIONAL DETAILS

The self-consistent LDA (Ref. 4) LAPW calculations were performed with the WIEN2K code[46] using a plane-wave cutoff of $k_{\max} R_{\mathrm{MT}} = 8$, with R_{MT} the smallest MT-sphere radius and $k_{\max}$ the largest k vector. The *N*MTO calculations were done with the Stuttgart code,[116] had $N = 1$, and all partial waves downfolded, except the TM *d* and O *p*.[47–50,52] The LAPW warped potential (spherical inside the LAPW MT spheres) was least-squares fitted to an overlapping MT potential with the recently developed OMTA code[58] and was used in the *N*MTO calculations. The radii of the hard screening spheres were 70% of the OMT radii.

The material-dependent settings are as follows:

NiO. Space group *Fm*-3*m* (225) $a = 4.177$ Å, Ni at Wyckoff position 4a and O at 4b. MT radii for Ni $2.08a_0$ and for O $1.84a_0$. $a_0 = 0.5292$ Å is the Bohr radius. OMT radii for Ni $2.2a_0$, for O $2.5a_0$, and for an additional empty sphere at Wyckoff position 8c $1.6a_0$. The expansion energies were −5.2 and −1.2 eV.

MnO. Space group *Fm*-3*m* (225) $a = 4.4248$ Å, Mn at Wyckoff position 4a, O at 4b. MT radii for Mn $2.20a_0$, and for O $1.95a_0$. OMT radii for Mn $2.3a_0$, for O $2.7a_0$, and for an additional empty sphere at Wyckoff position 8c $1.7a_0$. Expansion energies −5.0 and −1.0 eV.

SrTiO$_3$. Space group *Pm*-3*m* (221) $a = 3.905$ Å, Ti at Wyckoff position 1a, Sr at position 1b, and O at position 3d. MT radii for Ti $2.32a_0$, for Sr $2.00a_0$, and for O $1.36a_0$. OMT radii for Ti $2.4a_0$, for Sr $3.8a_0$, and for O $2.0a_0$. Expansion energies −2.6 and +1.5 eV.

The *N*MTO band structures and densities of states as presented in Figs. 2 and 5 were calculated from the real-space TM 3*d* O 2*p* Wannier-orbital (tight-binding) representation of the LDA Hamiltonian, neglecting hops between sites more distant than 2.5*a*. The tight-binding parameters larger than 10 meV are presented in the lower panels of Table I. Only

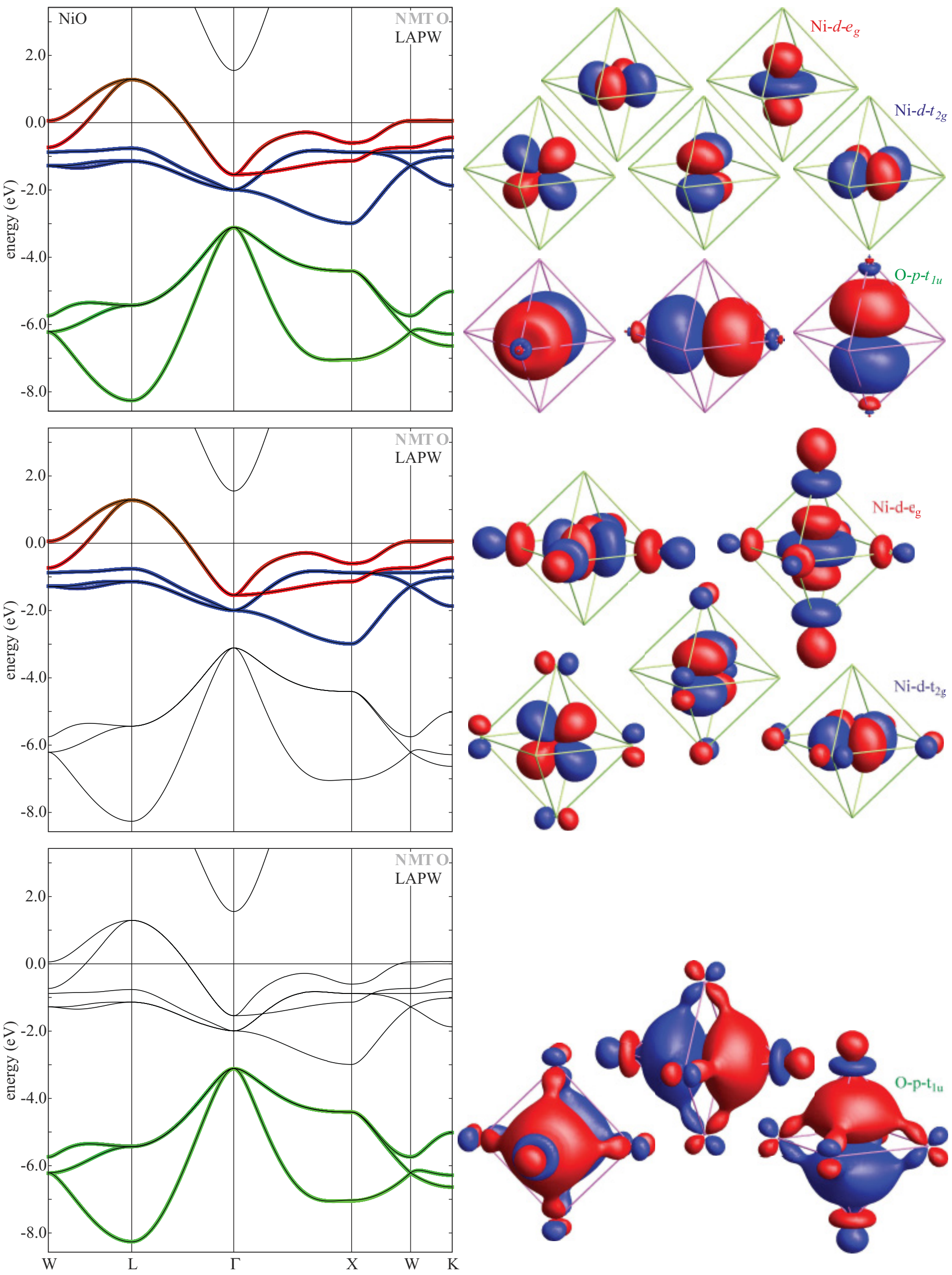

FIG. 11. (Color online) NiO band structure (left) and Wannier orbitals (right) for three different basis sets. Top panels: Including both the Ni d and O p orbitals. Middle panels: Including only the Ni d orbitals. Bottom panels: Including only the O p orbitals.

the nearest-neighbor hopping integrals (boldfaced) enter in the cluster calculations. In $SrTiO_3$, the point symmetry of O is merely tetragonal so that the p orbital pointing toward the Ti atom is slightly different from those pointing in directions perpendicular to the Ti-O bond (and, e.g., toward Sr). For a discussion of the bonding between the O p and Sr d orbitals and how this changes the different O p Wannier functions see Pavarini *et al.*[50] Due to the two different types of O p Wannier functions, the relation between the hopping integrals and the cubic ligand-field parameters is slightly more involved than those valid for O in cubic symmetry and given in Sec. II. In general (for all symmetries), the ligand-field parameters can be found by block tridiagonalization of the tight-binding Hamiltonian of the cluster with respect to the TM d orbitals. For more details see Appendix D.

Wannier orbitals have tails on the neighboring sites, although most of the orbital weight is close to the nucleus at its center (Fig. 3). The tails lead to long-ranged hopping integrals and their values are given in the lowest panels of Table I. It should be noticed that in order for MLFT to work properly with a basis set of LDA-based Wannier orbitals, it is important to have TM 3d atomiclike character for $r \lesssim 1.5$ Å, but it is not essential to have hopping limited to the first-nearest neighbors.

TABLE II. Multiplet ligand-field theory parameters taken from experiment. Note that the experiments shown in this paper are not very sensitive to these parameters. For a more thorough discussion on these parameters we refer to the papers by Bocquet *et al.* (Ref. 78) or Tanaka and Jo (Ref. 79). All values are in eV.

	$U_{3d,3d}$	Δ	$U_{2p,3d}$	$U_{3p,3d}$
NiO	7.3	4.7	8.5	—
MnO	5.5	8.0	7.2	5.5
$SrTiO_3$	6.0	6.0	8.0	—

The multipolar part of the Coulomb integrals is calculated by directly integrating the wave functions. In order to obtain numerically stable integrals, the Wannier orbitals were expanded in radial wave functions times spherical harmonics, an approximation for which a set of Slater integrals can be introduced. Sufficiently accurate results are obtained when different radial wave functions for the t_{2g} and e_g orbitals are used. The core wave functions, are calculated using the Hartree-Fock method.[61] For reasons of space, Table I only gives the Slater integrals for the radial functions averaged over t_{2g} and e_g; the difference between these integrals for NiO are given as an inset in Fig. 3. The spin-orbit coupling constants have been calculated using a spherical approximation, including only the local d character at the TM site. The resulting constant is the same for the t_{2g} and e_g orbitals.

The parameters fitted to experiments are shown in Table II. These values are in good agreement with those in the literature.[78,79] One should realize that since x-ray absorption involves a charge-neutral excitation, it is not very sensitive to U and Δ. The experiments discussed in this paper were chosen to be most sensitive to the calculated values (Table I).

The NMTO method[47–49] constructs the basis set of Ni d plus O p localized orbitals by first constructing such a set for *each* of the $N+1$ energies $\epsilon_0,\ldots,\epsilon_N$, chosen to span the energy range of interest. In such a set of zeroth-order ($N=0$) MTOs, each of the orbitals is a solution of Schrödinger's differential equation for the overlapping MT potential for the chosen energy, but has *kinks* at all Ni and O (but not, e.g., Sr) hard spheres.[117] Those hard spheres are chosen to be slightly smaller than touching distance and not to coincide with a node of the radial wave function. The Ni d_{xy} 0MTO, for instance, is now defined by the hard-sphere boundary condition that all its p projections on all O spheres and all its d projections on all Ni spheres, *except* d_{xy} on its *own* Ni sphere, *vanish;* And equivalently for the other members of the 0MTO basis set. This hard-sphere boundary condition is what localizes the 0MTOs, unless there are wave functions at the chosen energy with main characters different from those of the 0MTOs in the basis. The condition that each 0MTO solves Schrödinger's equation, except for kinks in the Ni d and O p channels, means that each 0MTO is smooth in all other channels. This is accomplished by constructing that set of wave-equation solutions in the hard-sphere interstitial, the so-called screened spherical waves, whose phase shifts are the hard-sphere ones for all Ni d and O p channels, except the eigenchannel, and have the proper phase shifts for all other channels (such as Ni s and Sr d). The screened spherical waves then get augmented inside the overlapping MT spheres to become the 0MTOs. Finally, the $N+1$ different 0MTO basis sets are contracted into one, the NMTO set, which spans the solutions of Schrödinger's equation at all $N+1$ energies. The NMTOs have discontinuities in merely the $(2N+1)$th derivatives at the hard spheres and are therefore smooth if $N>0$. The contraction (N-ization) delocalizes the NMTO to a degree which depends on how much the neighboring 0MTOs vary over the $N+1$ energies. This is so because, for an energy-independent set of orbitals, the energy dependence of a radial Schrödinger-equation solution must be provided by the tails of the neighboring orbitals.[42] The delocalization is further enhanced by symmetrical orthonormalization of the NMTOs into Wannier orbitals, and this depends on the overlap between neighboring NMTOs. Nevertheless, as seen in Fig. 2, our Ni d plus O p Wannier orbitals are as localized as can be expected, and—in fact—much better than Wannier orbitals derived from a large set of *energy-independent* orbitals.[118]

APPENDIX C: DOUBLE-COUNTING CORRECTION

DFT in the LDA already contains a large part of the local Coulomb interactions. These interactions are included once more in the MLFT calculations. For MLFT based on the LDA potential and Wannier orbitals one should therefore take care not to double-count such interactions. We differentiate rigidly between the monopole and the multipole parts of all Coulomb interactions. This idea is based on the experimental observation that the monopole part of the Coulomb interaction (U) is largely screened, from ~25 to ~7.3 eV in NiO for example. The multiplet splitting, determined by the multipole part of the Coulomb interaction is, however, only slightly reduced from the splitting one expects based on atomic values. This has for example been observed in Auger spectroscopy for the elemental 3d metals.[80]

The monopole part of the Coulomb interaction (U) as well as the spherical part of the on-site energy (Δ) we fit to the experiment and double counting for the spherical part is therefore not an issue. In order to prevent double counting of the multipole part of the Coulomb repulsion, the LDA calculations are done with a warped LDA potential; i.e., within the MT sphere only the spherical part of the potential is included. In order to check how this influences the LDA band structure we compare in Fig. 12 the band structures of NiO (top) and $SrTiO_3$ (bottom) calculated with the full LDA potential (thick) and warped MT potential (thin). Concentrating first on the NiO bands, we see that both calculations agree within basically the linewidth for all bands and **k** vectors, except for the t_{2g} bands. Those bands are shifted downward in the warped-MT calculations by a momentum-independent value of about 220 meV. This effect nicely illustrates the problem of double counting. The orbital occupation of the Ni 3d orbitals within the LDA is such that the t_{2g} orbitals are fully occupied and the e_g orbitals are half filled. The local charge density is thus cubic. The Coulomb repulsion between two t_{2g} orbitals is on average larger than between a t_{2g} and an e_g orbital. This effect is well included in the LDA functional and related to the fact that the overlap of, for example, the density of the d_{xy} and d_{xz} orbitals is larger than the overlap of the density of the d_{xy} and d_{3z^2-1} orbitals. In MLFT calculations, such interactions are included in the Slater integrals. A MLFT calculation based on the full LDA

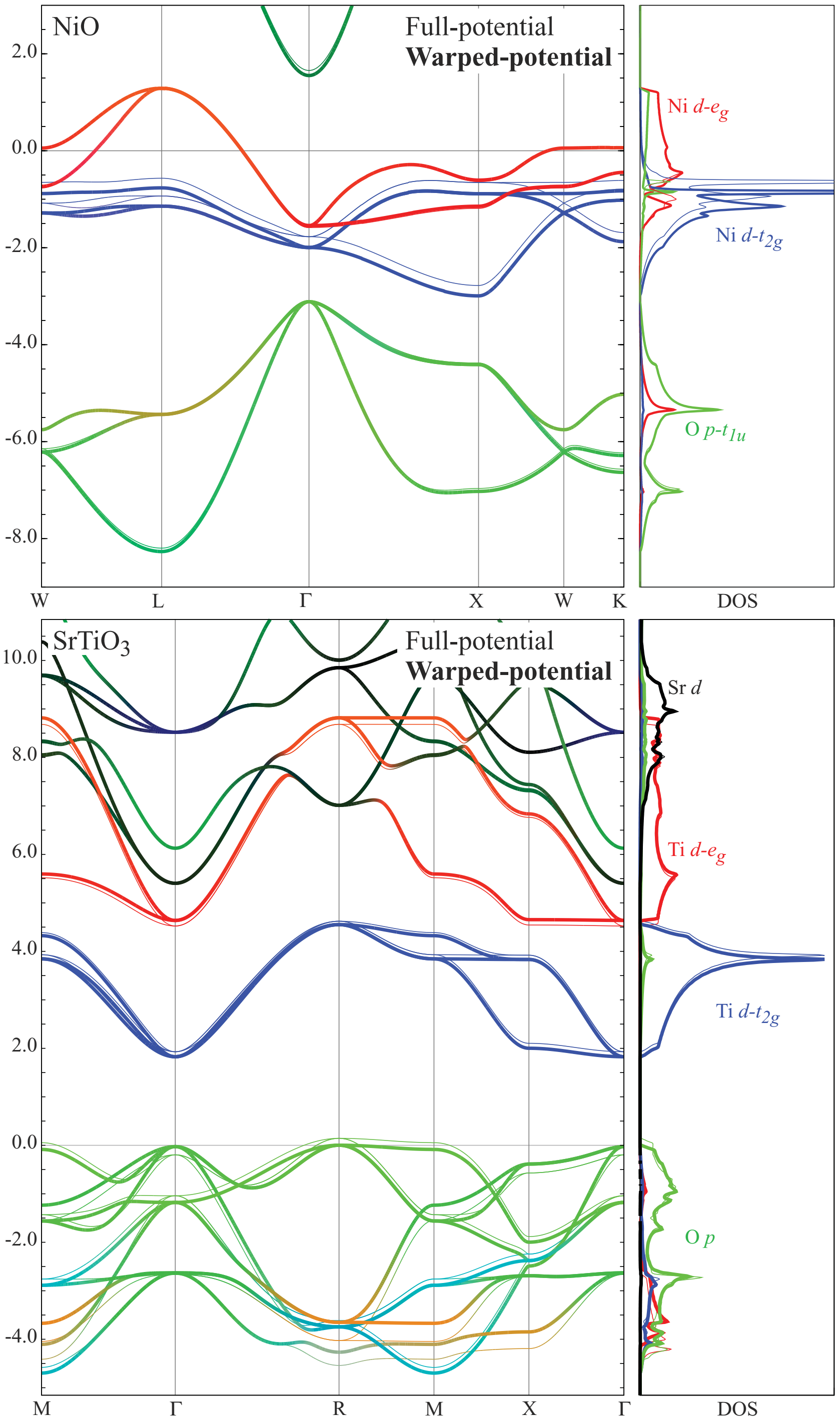

FIG. 12. (Color online) Comparison of the LAPW band structures and densities of states for the full LDA potential (thin lines) and the warped MT potential (thick lines). When only a single line can be seen, the two band structures overlap within the linewidth of the plot. The colors indicate the partial-wave characters inside the MT spheres.

potential would thus double-count the multipolar interaction between the fully occupied t_{2g} and the half-filled e_g shell.

One option would be to include the full potential within the LDA calculations and then subtract the nonspherical part of the Coulomb repulsion, as included in the LDA functional, between the Wannier functions for which a full multiplet interaction is included in the MLFT calculations. In that case one should carefully analyze the occupation of each Wannier function in order to determine the potential that has to be subtracted. We opted to not include the nonspherical interactions in the first place. This does mean that one also neglects the nonspherical part of the nonlocal Madelung potential in the self-consistent LDA calculations. In order to correct for this, we calculated this potential from the self-consistent LDA charge density and added it afterward. We found that the Coulomb potential which is double counted generally exceeds the nonspherical nonlocal potential by an order of magnitude. Our choice of not including the nonspherical interactions in the first place and treating the nonlocal nonspherical interactions as a correction after self-consistency has been reached thus provides an accurate self-consistent solution to the potential needed in MLFT. Nevertheless, we expect that doing a full-potential calculation and subsequently subtracting the nonspherical part of the local

Coulomb interaction according to the LDA functional will give very similar results.

In the bottom panel of Fig. 12 we compare the band structures of $SrTiO_3$ calculated for the warped and full potentials. First of all, there is no clear shift of the t_{2g} bands with respect to the e_g bands, presumably because Ti atom has a d^0 configuration. But there are changes in the O *p*-derived bands. In NiO both the Ni and the O atoms have cubic point symmetry, but in $SrTiO_3$ the O environment is tetragonal as was mentioned above. For $SrTiO_3$ one can see a larger difference between the full- and warped-potential calculations than for NiO. The interpretation for $SrTiO_3$ is less straightforward because several effects come together. Due to Ti-O covalency there is some nonspherical, predominantly e_g-derived charge on the Ti atom from the O $2p$ band. The local nonspherical potential due to this charge should not be included when doing MLFT calculations. There is, however, also a noncubic potential at the O site that shifts the O bands. This potential should be included when doing the MLFT calculations. Note that the latter potential is not included in the self-consistent warped-potential calculations, but we add it later, before doing the MLFT calculations.

APPENDIX D: BASIS-SIZE REDUCTION AND THE CREATION OF LIGAND ORBITALS BY BLOCK TRIDIAGONALIZATION

Embedded-cluster calculations, like those in MLFT or DMFT, contain a few correlated orbitals coupled to a large set of uncorrelated orbitals. Within such calculations the size of the Hilbert space can be reduced enormously by creating appropriate linear combinations of the uncorrelated orbitals. Within our examples these are the O *p* orbitals, which are combined with ligand orbitals. Without introducing ligand orbitals for an MO_6 cluster, there would be $(18 + 5) \times 2 = 46$ spin orbitals in the one-electron basis. With a filling of $8 + 6 \times 6 = 44$ electrons for the NiO_6 d^8 cluster, this results in $46!/(44! \times 2!) \sim 10^3$ states in the many-electron basis. For the TiO_6 d^0 cluster representing $SrTiO_3$, the filling would be $6 \times 6 = 36$ and thus result in $46!/(36! \times 10!) \sim 4 \times 10^9$ states in the many-electron basis. The introduction of L orbitals, however, reduces the number of one-electron basis functions to 20, whereby the many-electron Hilbert space is reduced to $20!/(18! \times 2!) = 190$ for a d^8 and to $20!/(10! \times 10!) \sim 2 \times 10^5$ states for a d^0 configuration. This reduction in the number of many-electron basis functions by factors of respectively $\frac{46!}{20!}\frac{(20-2)!}{(46-2)!} \sim 5$ and $\frac{46!}{20!}\frac{(20-10)!}{(46-10)!} \sim 22\,000$ leads to a crucial gain of computational convenience. Either basis set *can* be used to calculate ground-state properties and spectral functions because the matrices are sparse. But diagonalization of a matrix with dimension 4×10^9 requires large computational resources whereas diagonalization and evaluation of spectral functions of a sparse matrix with dimension 2×10^5 can be done using standard libraries on modern desktop computers. One may obtain a further reduction in the number of stored basis states by including only those which are important for representing the actual wave function (see Appendix E for details).

Ligand orbitals are normally obtained by symmetry considerations.[25] The rotation properties of the TM *d* orbitals should be the same as the linear combination of the O *p* orbitals with which this orbital makes a covalent bond. These symmetry considerations can be extended to a simple mathematical procedure, valid in all point-group symmetries. From DFT the one-particle Hamiltonian for an extended cluster is known on a basis of the central TM *d* orbitals and the neighbor O *p* orbitals. Using a block Lanczos routine one can create a unitary transformation of the *p* orbitals such that the one-particle Hamiltonian has a block tridiagonal form. The basis of the central TM *d* orbitals is not changed. In cubic symmetry the tridiagonalization results in a transformed Hamiltonian whereby each TM *d* orbital couples to one ligand orbital. For lower symmetries each *d* orbital couples to maximally five ligand orbitals. The ligand orbitals can couple to another set of ligand orbitals, *ad infinitum*. Covalence in a tridiagonal representation tends to converge fast, justifying the inclusion of only a single ligand shell in MLFT.

The introduction of ligand orbitals is not restricted to fully occupied shells, like the O p shell. For example, for $SrTiO_3$ one could include besides the O *p* ligand orbitals also the Sr *d* ligand orbitals. Care has to be taken in such a system as to the definition of the ligand orbitals. If one were to create a single ligand shell for both the O *p* and Sr *d* orbitals by block tridiagonalization as described in the previous paragraph, one would obtain ligand orbitals that are always partially occupied. This results in a very large many-particle basis set and is unpractical. In such a case it is better to first diagonalize the noninteracting Hamiltonian describing the interactions between the ligand orbitals. Based on the on-site energies one then creates two different ligand shells, one for the occupied or valence orbitals and one for the unoccupied or conduction orbitals.[119]

Note that a similar procedure can be used for DMFT calculations using a Lanczos impurity solver. Doing so enhances the calculation speed and allows one to increase the number of bath sites (the number of discretization sites used to represent the Anderson impurity model used in DMFT) leading to much more continuous spectral functions.

APPENDIX E: EXACT DIAGONALIZATION AND LANCZOS ALGORITHM

The MLFT ground-state and spectral calculations are done using a Lanczos algorithm.[22,23] The calculations start with a random vector (ψ_0) in the basis of the d^n and $d^{n+1}\underline{L}$ configurations, where n is the number of d electrons (zero for Ti, five for Mn, and eight for Ni) and $\underline{L}$ represents a single hole in the ligand shell. Although this starting point is slightly worse than the DFT single-Slater-determinant ground state, which prescribes a specific mixture of d and L states, it does contain the correct symmetry states. Thereby convergence is so fast that the starting point really does not matter much. Given a negative definite Hamiltonian, the wave function $\psi_1 = H\psi_0$ has a larger overlap with the ground-state wave function than does the wave function ψ_0. By repeatedly acting with the Hamiltonian on the random starting function and normalizing the wave function in between ($\psi_{n+1} = H\psi_n/|H\psi_n|$), one converges to the ground state. This procedure can be sped up considerably by creating a tridiagonal matrix of the Hamiltonian in the basis of ψ_n, with the additional constraint that ψ_{n+1} is orthogonal to ψ_n. The tridiagonal matrix in the so-called Krylov basis can be diagonalized with the use of dense matrix methods. Having found the ground state within the basis of the d^n plus $d^{n+1}\underline{L}$ configurations, we remove the basis functions not needed to represent the ground-state wave function from the basis and extend the basis set by acting with the Hamiltonian on the wave function. This creates basis states belonging to the $d^{n+2}\underline{L}^2$ configuration. Within this new basis set the ground state is found and the procedure of truncating and extending the basis set is repeated. The whole process is repeated until convergence is reached. Excited states are calculated by repeatedly orthogonalizing the wave function to the eigenstates already found. The algorithm as described here allows one to always keep relatively small basis sets.

Spectral functions are calculated by acting with the transition operator on the ground-state wave function. The resulting function is then used as a starting vector for the creation of a tridiagonal matrix in a Krylov basis. The spectral function of a tridiagonal matrix can be expressed in terms of a continued fraction.

---

[1] P. Hohenberg, and W. Kohn, Phys. Rev. **136**, B864 (1964).

[2] W. Kohn and L. J. Sham, Phys. Rev. **140**, A1133 (1965).

[3] W. Kohn, Rev. Mod. Phys. **71**, 1253 (1999).

[4] D. M. Ceperley and B. J. Alder, Phys. Rev. Lett. **45**, 566 (1980).

[5] J. P. Perdew, K. Burke, and M. Ernzerhof, Phys. Rev. Lett. **77**, 3865 (1996).

[6] V. I. Anisimov, J. Zaanen, and O. K. Andersen, Phys. Rev. B **44**, 943 (1991).

[7] V. I. Anisimov, I. V. Solovyev, M. A. Korotin, M. T. Czyzyk, and G. A. Sawatzky, Phys. Rev. B **48**, 16929 (1993).

[8] C. de Graaf, R. Broer, and W. C. Nieuwpoort, Chem. Phys. **208**, 35 (1996).

[9] A. Bande and A. Lüchow, Phys. Chem. Chem. Phys. **10**, 3371 (2008).

[10] L. Hozoi, U. Birkenheuer, H. Stoll, and P. Fulde, New J. Phys. **11**, 023023 (2009).

[11] P. Fulde, Adv. Phys. **51**, 909 (2002).

[12] F. Neese, T. Petrenko, D. Ganyushin, and G. Olbrich, Coord. Chem. Rev. **251**, 288 (2007).

[13] W. Metzner and D. Vollhardt, Phys. Rev. Lett. **62**, 324 (1989).

[14] A. Georges and G. Kotliar, Phys. Rev. B **45**, 6479 (1992).

[15] M. Jarrell, Phys. Rev. Lett. **69**, 168 (1992).

[16] A. Georges, G. Kotliar, W. Krauth, and M. J. Rozenberg, Rev. Mod. Phys. **68**, 13 (1996).

[17] V. I. Anisimov, A. I. Poteryaev, M. A. Korotin, A. O. Anokhin, and G. Kotliar, J. Phys.: Condens. Matter **9**, 7359 (1997).

[18] K. Held, I. A. Nekrasov, G. Keller, V. Eyert, N. Blümer, A. K. McMahan, R. T. Scalettar, Th. Pruschke, V. I. Anisimov, and D. Vollhardt, Psi-k Newsletter **56**, 65 (2003).

[19] T. Maier, M. Jarrell, T. Pruschke, and M. H. Hettler, Rev. Mod. Phys. **77**, 1027 (2005).

[20] F. Lechermann, A. Georges, A. Poteryaev, S. Biermann, M. Posternak, A. Yamasaki, and O. K. Andersen, Phys. Rev. B **74**, 125120 (2006).

[21] W. M. C. Foulkes, L. Mitas, R. J. Needs, and G. Rajagopal, Rev. Mod. Phys. **73**, 33 (2001).

[22] E. Dagotto, Rev. Mod. Phys. **66**, 763 (1994).

[23] A. Weiße, G. Wellein, A. Alvermann, and H. Fehske, Rev. Mod. Phys. **78**, 275 (2006).

[24] B. Lau, M. Berciu, and G. A. Sawatzky, Phys. Rev. Lett. **106**, 036401 (2011).

[25] C. J. Ballhausen, *Introduction to Ligand Field Theory* (McGraw-Hill, New York, 1962).

[26] S. Sugano and R. G. Shulman, Phys. Rev. **130**, 517 (1963).

[27] A. J. H. Wachters and W. C. Nieuwpoort, Int. J. Quantum Chem. **5**, 391 (1971).

[28] A. J. H. Wachters and W. C. Nieuwpoort, Phys. Rev. B **5**, 4291 (1972).

[29] *Nobel Lectures, Chemistry 1963–1970*, edited by R. S. Mulliken (Elsevier, Amsterdam, 1972).

[30] J. A. Pople, Rev. Mod. Phys. **71**, 1267 (1999).

[31] N. E. Brener and J. Callaway, Phys. Rev. B **35**, 4001 (1987).

[32] K. Ogasawara, T. Iwata, Y. Koyama, T. Ishii, I. Tanaka, and H. Adachi, Phys. Rev. B **64**, 115413 (2001).

[33] H. Ikeno, I. Tanaka, Y. Koyama, T. Mizoguchi, and K. Ogasawara, Phys. Rev. B **72**, 075123 (2005).

[34] H. Ikeno, T. Mizoguchi, Y. Koyama, Y. Kumagai, and I. Tanaka, Ultramicroscopy **106**, 970 (2006).

[35] H. Ikeno, R. M. F. de Groot, E. Stavitski, and I. Tanaka, J. Phys.: Condens. Matter **21**, 104208 (2009).

[36] P. S. Miedema, H. Ikeno, and F. M. F. de Groot, J. Phys.: Condens. Matter **23**, 145501 (2011).

[37] H. Ikeno, T. Mizoguchi, Y. Koyama, Z. Ogumi, Y. Uchimoto, and I. Tanaka, J. Phys. Chem. C **115**, 11871 (2011).

[38] C. de Graaf, W. A. de Jong, R. Broer, and W. C. Nieuwpoort, Chem. Phys. **237**, 59 (1998).

[39] M. Geleijns, C. de Graaf, R. Broer, and W. C. Nieuwpoort, Surf. Sci. **421**, 106 (1999).

[40] A. Sadoc, R. Broer, and C. de Graaf, J. Chem. Phys. **126**, 134709 (2007).

[41] L. Hozoi, L. Siurakshina, P. Fulde, and J. van den Brink, Scientific Reports **1**, 65 (2011).

[42] O. K. Andersen, Phys. Rev. B **2**, 883 (1970).

[43] O. Gunnarsson, O. K. Andersen, O. Jepsen, and J. Zaanen, Phys. Rev. **39**, 1708 (1989).

[44] V. I. Anisimov and O. Gunnarsson, Phys. Rev. B **43**, 7570 (1991).

[45] O. K. Andersen, Phys. Rev. B **12**, 3060 (1975).

[46] P. Blaha, K. Schwarz, P. Sorantin, and S. B. Trickey, Comput. Phys. Commun. **59**, 399 (1990).

[47] O. K. Andersen and T. Saha-Dasgupta, Phys. Rev. B **62**, R16219 (2000).

[48] O. K. Andersen, T. Saha-Dasgupta, S. Ezhov, L. Tsetseris, O. Jepsen, R. W. Tank, C. Arcangeli, and G. Krier, Psi-k Newsletter **45**, 86 (2001).

[49] O. K. Andersen and T. Saha-Dasgupta, and S. Ezhov, Bull. Mater. Sci. **26**, 19 (2003).

[50] E. Pavarini, A. Yamasaki, J. Nuss, and O. K. Andersen, New J. Phys. **7**, 188 (2005).

[51] A. Yamasaki, M. Feldbacher, Y.-F. Yang, O. K. Andersen, and K. Held, Phys. Rev. Lett. **96**, 166401 (2006).

[52] E. Zurek, O. Jepsen, and O. K. Andersen, ChemPhysChem. **6**, 1934 (2005).

[53] E. Sjoestedt, L. Nordstroem, and D. J. Singh, Solid State Commun. **114**, 15 (2000).

[54] L. F. Mattheiss, Phys. Rev. B **5**, 290 (1972).

[55] F. J. Morin, Phys. Rev. **93**, 1199 (1954).

[56] R. Newman and R. M. Chrenko, Phys. Rev. **114**, 1507 (1959).

[57] R. J. Powell and W. E. Spicer, Phys. Rev. B **2**, 2182 (1970).

[58] M. Zwierzycki and O. K. Andersen, Acta Phys. Pol. A **115**, 64 (2009).

[59] We used $N = 1$. Note that even with this value, the NMTO method (Ref. 47) is far more physical, flexible, and accurate than the conventional linear muffin-tin orbital method (Ref. 60).

[60] O. K. Andersen and O. Jepsen, Phys. Rev. Lett. **53**, 2571 (1984).

[61] R. D. Cowan, *The Theory of Atomic Structure and Spectra* (University of California Press, Berkeley, 1981).

[62] J. Kuneš, R. Arita, P. Wissgott, A. Toschi, H. Ikeda, and K. Held, Comput. Phys. Commun. **181**, 1888 (2010).

[63] Note that in multiplet ligand-field theory the covalent interaction of the t_{2g} and e_g orbitals with the ligands is taken explicitly into account and is therefore *not* included in the t_{2g}-e_g splitting $10Dq$. On the other hand, in multiplet crystal-field theory the difference in covalency of the t_{2g} and e_g orbitals with the ligands ($pd\pi$ and $pd\sigma$, respectively) is included in the splitting $10Dq$, so that this is a different quantity in MCFT. Said in another way: MLFT uses a basis set of TM d plus ligand p Wannier orbitals, while MCFT uses a basis set of only TM d Wannier orbitals, which therefore have the antibonding ligand p character downfolded into their tails.

[64] J. Ghijsen, L. H. Tjeng, J. van Elp, H. Eskes, J. Westerink, G. A. Sawatzky, and M. T. Czyzyk, Phys. Rev. B **38**, 11322 (1988).

[65] H. Eskes, L. H. Tjeng, and G. A. Sawatzky, Phys. Rev. B **41**, 288 (1990).

[66] O. K. Andersen, W. Klose, and H. Nohl, Phys. Rev. B **17**, 1209 (1978).

[67] V. I. Anisimov, D. E. Kondakov, A. V. Kozhevnikov, I. A. Nekrasov, Z. V. Pchelkina, J. W. Allen, S.-K. Mo, H.-D. Kim, P. Metcalf, S. Suga, A. Sekiyama, G. Keller, I. Leonov, X. Ren, and D. Vollhardt, Phys. Rev. B **71**, 125119 (2005).

[68] L. Cano-Cortés, A. Dolfen, J. Merino, J. Behler, B. Delley, K. Reuter, and E. Koch, Eur. Phys. J. B **56**, 173 (2007).

[69] V. I. Anisimov, D. M. Korotin, M. A. Korotin, A. V. Kozhevnikov, J. Kuneš, A. O. Shorikov, and S. L. Skornyakov, and S. V. Streltsov, J. Phys.: Condens. Matter **21**, 075602 (2009).

[70] T. Miyake, K. Nakamura, R. Arita, and M. Imada, J. Phys. Soc. Jpn. **79**, 044705 (2010).

[71] E. Şaşioğlu, C. Friedrich, and S. Blü gel, Phys. Rev. B **83**, 121101(R) (2011).

[72] A. K. McMahan, R. M. Martin, and S. Satpathy, Phys. Rev. B **38**, 6650 (1988).

[73] M. S. Hybertsen and M. Schluter, and N. E. Christensen, Phys. Rev. B **39**, 9028 (1989).

[74] M. Cococcioni and S. de Gironcoli, Pys. Rev. B **71**, 035105 (2005).

[75] M. Springer and F. Aryasetiawan, Phys. Rev. B **57**, 4364 (1998).

[76] F. Aryasetiawan, M. Imada, A. Georges, G. Kotliar, S. Biermann, and A. I. Lichtenstein, Phys. Rev. B **70**, 195104 (2004).

[77] C. Franchini, R. Kovacik, M. Marsman, S. Sathyanarayana Murthy, J. He, C. Ederer, and G. Kresse, e-print arXiv:1111.1528.

[78] A. E. Bocquet, T. Mizokawa, K. Morikawa, A. Fujimori, S. R. Barman, K. Maiti, D. D. Sarma, Y. Tokura, and M. Onoda, Phys. Rev. B **53**, 1161 (1996).

[79] A. Tanaka and T. Jo, J. Phys. Soc. Jpn. **63**, 2788 (1994).

[80] E. Antonides, E. C. Janse, and G. A. Sawatzky, Phys. Rev. B **15**, 1669 (1977).

[81] F. de Groot and A. Kotani, *Core Level Spectroscopy of Solids* (CRC Press, New York, 2008).

[82] J. Stöhr, *NEXAPS Spectroscopy* (Springer, Berlin, 1992).

[83] W. Schülke, *Electron Dynamics by Inelastix X-Ray Scattering* (Oxford University Press, Oxford, 2007).

[84] Y. Uehara, D. W. Lindle, T. A. Callcott, L. T. Terminello, F. J. Himpsel, D. L. Ederer, J. H. Underwood, E. M. Gullikson, and R. C. C. Perera, Appl. Phys. A **65**, 179 (1997).

[85] S. I. Csiszar, M. W. Haverkort, T. Burnus, A. Tanaka, H. H. Hsieh, H.-J. Lin, C. T. Chen, J. C. Cezar, N. B. Brookes, T. Hibma, and L. H. Tjeng, e-print arXiv:cond-mat/0504520.

[86] S. I. Csiszar, M. W. Haverkort, Z. Hu, A. Tanaka, H. H. Hsieh, H. J. Lin, C. T. Chen, T. Hibma, and L. H. Tjeng, Phys. Rev. Lett. **95**, 187205 (2005).

[87] D. Alders, L. H. Tjeng, F. C. Voogt, T. Hibma, G. A. Sawatzky, C. T. Chen, J. Vogel, M. Sacchi, and S. Iacobucci, Phys. Rev. B **57**, 11623 (1998).

[88] F. M. F. de Groot, J. C. Fuggle, B. T. Thole, and G. A. Sawatzky, Phys. Rev. B **41**, 928 (1990).

[89] J. Fink, Th. Müller-Heinzerling, B. Scheerer, W. Speier, F. U. Hillebrecht, J. C. Fuggle, J. Zaanen, and G. A. Sawatzky, Phys. Rev. B **32**, 4899 (1985).

[90] F. M. F. de Groot, J. C. Fuggle, B. T. Thole, and G. A. Sawatzky, Phys. Rev. B **42**, 5459 (1990).

[91] C. T. Chen, L. H. Tjeng, J. Kwo, H. L. Kao, P. Rudolf, F. Sette, and R. M. Fleming, Phys. Rev. Lett. **68**, 2543 (1992).

[92] B. T. Thole, G. van der Laan, and G. A. Sawatzky, Phys. Rev. Lett. **55**, 2086 (1985).

[93] J. B. Goedkoop, B. T. Thole, G. van der Laan, G. A. Sawatzky, F. M. F. de Groot, and J. C. Fuggle, Phys. Rev. B **37**, 2086 (1988).

[94] G. van der Laan, J. Zaanen, G. A. Sawatzky, R. Karnatak, and J.-M. Esteva, Phys. Rev. B **33**, 4253 (1986).

[95] E. Benckiser, M. W. Haverkort, S. Brück, E. Goering, S. Macke, A. Fraňó, X. Yang, O. K. Andersen, G. Cristiani, H.-U. Habermeier, A. V. Boris, I. Zegkinoglou, P. Wochner, H.-J. Kim, V. Hinkov, and B. Keimer, Nat. Mater. **10**, 189 (2011).

[96] M. W. Haverkort, Phys. Rev. Lett. **105**, 167404 (2010).

[97] S. Glawion, J. Heidler, M. W. Haverkort, L. C. Duda, T. Schmitt, V. N. Strocov, C. Monney, K. J. Zhou, A. Ruff, M. Sing, and R. Claessen, Phys. Rev. Lett. **107**, 107402 (2011).

[98] P. Krüger and C. R. Natoli, Phys. Rev. B **70**, 245120 (2004).

[99] P. Krüger, Phys. Rev. B **81**, 125121 (2010).

[100] R. Laskowski and P. Blaha, Phys. Rev. B **82**, 205104 (2010).

[101] S. Altieri, L. H. Tjeng, A. Tanaka, and G. A. Sawatzky, Phys. Rev. B **61**, 13403 (2000).

[102] J. Kuneš, V. I. Anisimov, S. L. Skornyakov, A. V. Lukoyanov, and D. Vollhardt, Phys. Rev. Lett. **99**, 156404 (2007).

[103] J. Kuneš, V. I. Anisimov, A. V. Lukoyanov, and D. Vollhardt, Phys. Rev. B **75**, 165115 (2007).

[104] R. Eder, Phys. Rev. B **78**, 115111 (2008).

[105] M. A. van Veenendaal and G. A. Sawatzky, Phys. Rev. Lett. **70**, 2459 (1993).

[106] K. Hämäläinen, S. Galambosi, J. A. Soininen, E. L. Shirley, J.-P. Rueff, and A. Shukla, Phys. Rev. B **65**, 155111 (2002).

[107] M. W. Haverkort, A. Tanaka, L. H. Tjeng, and G. A. Sawatzky, Phys. Rev. Lett. **99**, 257401 (2007).

[108] R. W. Gordon, G. T. Seidler, T. T. Fister, M. W. Haverkort, G. A. Sawatzky, A. Tanaka, and T. K. Sham, Europhys. Lett. **81**, 26004 (2008).

[109] R. A. Gordon, M. W. Haverkort, S. S. Gupta, and G. A. Sawatzky, J. Phys.: Conf. Ser. **190**, 012047 (2009).

[110] S. Sen Gupta, J. A. Bradley, M. W. Haverkort, G. T. Seidler, A. Tanaka, and G. A. Sawatzky, Phys. Rev. B **84**, 075134 (2011).

[111] B. C. Larson, J. Z. Tischler, Wei Ku, Chi-Cheng Lee, O. D. Restrepo, A. G. Eguiluz, P. Zschack, and K. D. Finkelstein, Phys. Rev. Lett. **99**, 026401 (2007).

[112] R. Verbeni, T. Pylkkaenen, S. Huotari, L. Simonelli, G. Vanko, K. Martel, C. Henriquet, and G. Monaco, J. Synchrotron Radiat. **16**, 469 (2009).

[113] N. Hiraoka, M. Suzuki, K. D. Tsuei, H. Ishii, Y. Q. Cai, M. W. Haverkort, C. C. Lee, and W. Ku, Euro. Phys. Lett. **96**, 37007 (2011).

[114] Michel van Veenendaal and M. W. Haverkort, Phys. Rev. B **77**, 224107 (2008).

[115] C.-C. Lee, H. C. Hsueh, and W. Ku, Phys. Rev. B **82**, 081106 (2010).

[116] The Stuttgart tight-binding linear muffin-tin orbital atomic-sphere approximation code, version 4.7; [http://www.fkf.mpg.de/andersen/].

[117] The proper wave functions at the chosen energy are those linear combinations for which the kinks cancel.

[118] I. V. Solovyev, Z. V. Pchelkina, and V. I. Anisimov, Phys. Rev. B **75**, 045110 (2007).

[119] O. Gunnarsson and K. Schönhammer, Phys. Rev. B **28**, 4315 (1983).